

12

AD A120243

# Electromagnetic Properties and Communication Characteristics of PACSAT

Edward Bedrosian

DTIC  
SELECTED  
OCT 13 1982  
H

DTIC FILE COPY

This document has been approved  
for public release and sale; its  
distribution is unlimited.

**Rand**

82 10 13 005

The research described in this report was sponsored by the Defense Advanced Research Projects Agency under ARPA Order No. 3584-5, Contract No. MDA903-78-C-0281, Strategic Technology Office.

ISBN 0-8330-0439-5

LC Card No. 82-16500

**The Rand Publications Series:** The Report is the principal publication documenting and transmitting Rand's major research findings and final research results. The Rand Note reports other outputs of sponsored research for general distribution. Publications of The Rand Corporation do not necessarily reflect the opinions or policies of the sponsors of Rand research.

**Published by The Rand Corporation**

Calculators for R-2920-ARPA,  
Electromagnetic Properties and Communication Characteristics  
of PACSAT

Three calculators have been developed to supplement the plots and calculations presented in this report.

(1) Passive Satellite Calculator. This calculator is a circular slide rule that permits numerical evaluations of typical passive-satellite link parameters. It solves Eq. (4.25) to produce results such as those listed in Table 4.4.

(2) Satellite Range Calculator. This (and the following) calculator uses the polar stereographic projection of the Northern Hemisphere shown in Fig. 4.5 to calculate the slant range from a satellite in a circular equatorial orbit to an arbitrary point within its field of view. A set of overlays covers the range of orbital altitudes from 3000 to 10,000 km. Unlike Fig. 4.12, which is based on relative satellite and user location, this slide rule uses actual geographical locations and facilities visualizing the coverage area.

(3) Satellite Coverage Calculator. Using the same projection and satellite orbits as the Range Calculator, this calculator uses a pair of overlays, similar to Fig. 4.4, to depict the extremes of satellite longitudes for mutual visibility between a specific user pair or for users within a given user area. Auxiliary scales yield the arc of mutual visibility and the mutual viewing time for a generalized pair of users (Figs. 4.7 and 4.8 give these quantities for specific user pairs).

The Passive Satellite Calculator is general in that it can be used over a wide range of parameters for a passive satellite system with no restrictions on the orbit. The Satellite Range and Coverage Calculators are specific for satellites, whether active or passive, in circular equatorial orbits. These calculators are available at cost from The Rand Corporation. Inquiries should be directed to the Engineering and Applied Sciences Department.

REPORT DOCUMENTATION PAGE		READ INSTRUCTIONS BEFORE COMPLETING FORM
1. REPORT NUMBER R-2920-ARPA	2. GOVT ACCESSION NO. A120 243	3. RECIPIENT'S CATALOG NUMBER
4. TITLE (and Subtitle) Electromagnetic Properties and Communication Characteristics of PACSAT		5. TYPE OF REPORT & PERIOD COVERED Interim
		6. PERFORMING ORG. REPORT NUMBER
7. AUTHOR(s) Edward Bedrosian		8. CONTRACT OR GRANT NUMBER(s) MDA903-78-C-0281
9. PERFORMING ORGANIZATION NAME AND ADDRESS The Rand Corporation 1700 Main Street Santa Monica, CA 90406		10. PROGRAM ELEMENT, PROJECT, TASK AREA & WORK UNIT NUMBERS
11. CONTROLLING OFFICE NAME AND ADDRESS Defense Advanced Research Projects Agency Department of Defense Arlington, Virginia 22209		12. REPORT DATE August 1982
		13. NUMBER OF PAGES 97
14. MONITORING AGENCY NAME & ADDRESS (if different from Controlling Office)		15. SECURITY CLASS. (of this report) Unclassified
		15a. DECLASSIFICATION/DOWNGRADING SCHEDULE
16. DISTRIBUTION STATEMENT (of this Report)  Approved for Public Release; Distribution Unlimited		
17. DISTRIBUTION STATEMENT (of the abstract entered in Block 20, if different from Report)  No Restrictions		
18. SUPPLEMENTARY NOTES		
19. KEY WORDS (Continue on reverse side if necessary and identify by block number)  Communication Satellites Missiles Command and Control		
20. ABSTRACT (Continue on reverse side if necessary and identify by block number)  See Reverse Side		

UNCLASSIFIED

SECURITY CLASSIFICATION OF THIS PAGE(When Data Entered)

↓  
This report

→ Presents an analysis of various technical and system properties of a passive communication satellite concept known as PACSAT. The satellite is a linear array of scatterers oriented toward the center of the earth by the gravity-gradient force. The scatterers are assumed to consist of perfectly conducting spheres that are uniformly spaced. First the scattering cross section of the array is developed and the effects of flexure and near-field operation are considered. The array is then assumed to be in a circular equatorial orbit and various system and orbit parameters are calculated for users in a service area approximating the United States in shape. Finally, communication characteristics are investigated and power budgets presented for typical system configurations.

UNCLASSIFIED

SECURITY CLASSIFICATION OF THIS PAGE(When Data Entered)

R-2920-ARPA

# **Electromagnetic Properties and Communication Characteristics of PACSAT**

Edward Bedrosian

August 1982

Prepared for the  
Defense Advanced Research Projects Agency



## PREFACE

This report presents an analysis of various technical and system properties of a passive communication satellite concept known as PACSAT. Included are electromagnetic scattering, orbital and geometrical considerations, and communication characteristics. A general description of PACSAT and its potential application to the command and control of strategic forces is given in a companion Rand Note: Edward Bedrosian, *PACSAT: A Passive Communication Satellite for Survivable Command and Control*, N-1780-ARPA, November 1981.

The research reported here was sponsored by the Strategic Technology Office, Defense Advanced Research Projects Agency (contract MDA 903-78-C-0281), under the supervision of Dr. Sherman Karp. It is an element of a broad range of strategic communication studies being conducted for DARPA by Rand.

[illegible]

SUMMARY

This report presents a detailed electromagnetic and communication system analysis of a passive communication satellite known as PACSAT. The satellite is a linear array of scatterers oriented toward the center of the earth by the gravity-gradient force. The scatterers are assumed to consist of uniformly spaced, perfectly conducting spheres.

First, the scattering cross section of the array is developed and the effects of flexure and near-field operation are considered. The array is then assumed to be in a circular equatorial orbit and various system and orbital parameters are calculated for users in a service area approximating the United States in shape. Finally, communication characteristics are investigated and power budgets presented for typical system configurations.



ACKNOWLEDGMENTS

The numerical calculations of the Mie solution to scattering from a sphere were performed by V. V. Liepa of the Radiation Laboratory at the University of Michigan. His generous cooperation is gratefully acknowledged. The author is also indebted to Drs. Richard Frick, Irving S. Reed (consultant), and William Sollfrey of Rand for their many helpful discussions.

CONTENTS

PREFACE .....	iii
SUMMARY .....	v
ACKNOWLEDGMENTS .....	vii
FIGURES .....	xi
TABLES .....	xv
GLOSSARY .....	xvii
Section	
I. SYNOPSIS .....	1
II. ELECTROMAGNETIC PROPERTIES IN THE FAR FIELD .....	6
Far-Field Scattering from a Sphere .....	6
Gain of the Array in the Far Field .....	14
Far-Field Scattering from the Array .....	21
Directivity Pattern in the Far Field .....	24
III. QUADRATIC PHASE ERROR EFFECTS .....	30
The Dofocusing Parameter .....	30
Near-Field Operation and Array Flexure .....	36
IV. PACSAT IN A CIRCULAR EQUATORIAL ORBIT .....	51
Geometrical and Orbital Properties .....	52
Array Operating Parameters .....	66
Communication Characteristics .....	78
Appendix: FIFTH-ORDER R.M.S. POLYNOMIAL FIT TO MIE SOLUTION EXPANSION FOR ELECTROMAGNETIC SCATTERING FROM A PER- FECTLY CONDUCTING SPHERE .....	83
REFERENCES .....	85

FIGURES

1.1. The PACSAT communication link .....	2
2.1. Geometry of field scattered from a sphere .....	7
2.2. Scattering from a sphere of radius $a$ at wavelength $\lambda$ .....	13
2.3. The normalized radar or backscattering cross section of a perfectly conducting sphere .....	14
2.4. The basic PACSAT array .....	15
2.5. Plots of integrand of Eq. (2.32) for $\alpha = \beta_1 = \pi/6$ .....	19
2.6. Scattering from the PACSAT array of length $L$ at wa- length $\lambda$ .....	22
2.7. Optimum scattering from the PACSAT array .....	23
2.8. Normalized 3 dB beamwidth of PACSAT array .....	27
2.9. Far-field directivity pattern of PACSAT array .....	29
3.1. Directivity pattern of defocused PACSAT array .....	34
3.2. Scattering cross section loss for the defocused PACSAT array .....	35
3.3. Geometry of PACSAT in orbit when tilted and flexed .....	37
3.4. Geometry of the flexed array .....	41
3.5. Simplified geometry of the tilted and flexed array .....	45
3.6. Near-worst-case, flexure/length tradeoff: users at 38 deg latitude separated 38 deg in longitude and array at midlongitude over equator .....	48
3.7. Normalized array length .....	49
4.1. Link geometry for PACSAT in a circular equatorial orbit ..	53
4.2. Orbital period for a satellite in a circular orbit .....	54
4.3. Orbital angular rate relative to the earth for a satellite in a circular equatorial orbit .....	55

4.4.	Coverage contours for a satellite in an equatorial orbit .....	57
4.5.	Generalized service area and user locations chosen to illustrate significant system parameters .....	59
4.6a.	Azimuth and elevation trajectories for a satellite in a circular equatorial orbit as viewed by a user at 30 deg N latitude .....	60
4.6b.	Azimuth and elevation trajectories for a satellite in a circular equatorial orbit as viewed by a user at 45 deg N latitude .....	61
4.7a.	Arc of mutual visibility for a satellite in a circular equatorial orbit as viewed by users both at 30 deg latitude .....	62
4.7b.	Arc of mutual visibility for a satellite in a circular equatorial orbit as viewed by one user at 30 deg latitude and the other at 45 deg latitude .....	63
4.7c.	Arc of mutual visibility for a satellite in a circular equatorial orbit as viewed by users both at 45 deg latitude .....	63
4.8a.	Mutual viewing time for a satellite in a circular equatorial orbit as viewed by users both at 30 deg latitude .....	64
4.8b.	Mutual viewing time for a satellite in a circular equatorial orbit as viewed by one user at 30 deg latitude and the other at 45 deg latitude .....	65
4.8c.	Mutual viewing time for a satellite in a circular equatorial orbit as viewed by users both at 45 deg latitude .....	65
4.9a.	Bistatic scattering angle for a satellite in a circular equatorial orbit as viewed by users both at 30 deg latitude and separated by 45 deg in longitude .....	66
4.9b.	Bistatic scattering angle for a satellite in a circular equatorial orbit as viewed by one user at 30 deg latitude and the other at 45 deg latitude, separated by 45 deg in longitude .....	67
4.9c.	Bistatic scattering angle for a satellite in a circular equatorial orbit as viewed by users both at 45 deg latitude and separated by 45 deg in longitude .....	67

4.10a.	Extremes of operating wavelength and frequency for a librating PACSAT in a circular equatorial orbit as viewed by users both at 30 deg latitude and separated by 45 deg in longitude .....	69
4.10b.	Extremes of operating wavelength and frequency for a librating PACSAT in a circular equatorial orbit as viewed by one user at 30 deg latitude and the other 45 deg latitude, separated by 45 deg in longitude ....	70
4.10c.	Extremes of operating wavelength and frequency for a librating PACSAT in a circular equatorial orbit as viewed by users both at 45 deg latitude and separated by 45 deg in longitude .....	70
4.11a.	Normalized scattering cross section for a nonlibrating PACSAT in a circular equatorial orbit as viewed by users both at 30 deg latitude and separated by 45 deg in longitude .....	74
4.11b.	Normalized scattering cross section for a nonlibrating PACSAT in a circular equatorial orbit as viewed by one user at 30 deg latitude and the other at 45 deg latitude, separated by 45 deg in longitude .....	75
4.11c.	Normalized scattering cross section for a nonlibrating PACSAT in a circular equatorial orbit a viewed by users both at 45 deg latitude and separated by 45 deg in longitude .....	75
4.12.	Line-of-sight path length to a satellite in an equatorial orbit .....	79

TABLES

4.1. Typical Generalized PACSAT Design Parameters .....	74
4.2. Typical Specific PACSAT Design Parameters .....	76
4.3. Typical PACSAT System Parameters .....	77
4.4. Typical PACSAT Link Parameters .....	82

# GLOSSARY

The defining equation (in italics) or the equation of first reference is given at the right. Figure numbers are given when appropriate. Unit vectors are formed by placing bars over the appropriate coordinate designation.

## English

A	azimuth of line of sight	<i>Eq. (4.6)</i>	Fig. 4.1
$A_{eff}$	effective area	<i>Eq. (2.35)</i>	
$A_n$	coefficient of nth term in Mie series expansion	<i>Eq. (2.5)</i>	
a	sphere radius	<i>Eq. (2.5)</i>	
$a_{xy}$	scattering coefficient, y to x polarization	<i>Eq. (2.11)</i>	
$B_n$	coefficient of nth term in Mie expansion	<i>Eq. (2.5)</i>	
$C(z)$	cosine Fresnel integral	<i>Eq. (3.12)</i>	
$c_n$	coefficient of nth term in array length expansion	<i>Eq. (3.2)</i>	
D	maximum deflection of flexed array	<i>Eq. (3.29)</i>	Fig. 3.4
D	diameter of parabolic dish	<i>Eq. (4.24)</i>	
D	directivity pattern	<i>Eq. (2.42)</i>	
$\mathcal{A}$	normalized flexure parameter	<i>Eq. (3.33)</i>	
$d_k$	distance from array center to kth element	<i>Eq. (3.20)</i>	Fig. 3.3
$ E $	magnitude of electric field vector	<i>Eq. (2.19)</i>	
E	elevation angle of line of sight	<i>Eq. (4.8)</i>	Fig. 4.1
$E_p$	received energy per bit	<i>Eq. (4.19)</i>	
$\bar{E}^i$	incident electric field vector	<i>Eq. (2.1)</i>	
$\bar{E}^s$	scattered electric field vector	<i>Eq. (2.3)</i>	
$f_1$	frequency to direct first-order grating lobe toward receiver	<i>Eq. (2.57)</i>	
$f_{3dB}$	3 dB beamwidth in frequency	<i>Eq. (2.58)</i>	
G	array gain	<i>Eq. (2.27)</i>	

$G_T, G_R$	antenna gain	Eq. (4.22)	
$h$	orbital altitude (above surface of earth)	Eq. (3.17)	
$h$	geometrical parameter	Eq. (3.25)	
$h_n^{(1)}$	spherical Bessel function of the third kind	Eq. (2.6)	
$J$	defined integral	Eq. (2.30)	
$j$	geometrical parameter	Eq. (3.25)	
$j_n$	real part of spherical Bessel function of third kind	Eq. (2.6)	
$k$	order of grating lobe	Eq. (2.22)	
$k$	index to kth array element	Eq. (3.2)	
$k$	Boltzmann's constant ( $1.38054 \times 10^{-3} \text{ J/}^\circ\text{K}$ )	Eq. (4.18)	
$k_0$	wavelength parameter	Eq. (2.1)	
$L$	array length	Eq. (2.39)	
$L$	link loss factor	Eq. (4.17)	
$L_k$	path length from transmitter to receiver via kth element	Eq. (3.1)	
$L$	projected array length	Eq. (3.29)	Fig. 3.4
$l_k$	path length to kth element	Eq. (3.20)	Fig. 3.3
$M$	system margin	Eq. (4.21)	
$N$	number of elements in array	Eq. (2.19)	
$N_0$	system noise spectral density	Eq. (4.18)	
$P_R, P_T$	received and transmitted powers	Eq. (4.17)	
$P_n^1$	associated Legendre function	Eq. (2.4)	
$R_R, R_T$	line-of-sight path lengths to receiver and transmitter	Eq. (4.17)	
$R_e$	radius of the earth (6378 km)	Eq. (3.17)	Fig. 3.3
$r$	distance to reference field point	Eq. (2.3)	Fig. 2.1
$r$	radius of orbit	Eq. (4.1)	
$S(z)$	sine Fresnel integral	Eq. (3.12)	
$S_1, S_2$	functions in Mie series expansion	Eq. (2.4)	
$Si$	sine integral	Eq. (2.33)	
$s$	array element spacing	Eq. (1.1)	
$s_k$	distance along array to kth element	Eq. (3.27)	Fig. 3.4



$T$	system noise temperature	Eq. (4.18)	
$t$	time	Eq. (2.1)	
$t$	running variable along array	Eq. (3.28)	
$U$	defocusing parameter	Eq. (3.15)	
$U_1, U_2$	generalized defocusing parameters	Eq. (3-11)	
$u$	integration parameter	Eq. (2.31)	
$v$	integration parameter	Eq. (2.31)	
$x$	expansion parameter	Eq. (2.21)	
$x_k$	projected distance to kth element	Eq. (3.34)	Fig. 3.4
$y$	wavelength directivity parameter	Eq. (2.47)	
$y_k$	projected distance to kth element	Eq. (3.35)	Fig. 3.4
$y_n$	imaginary part of spherical Bessel function of third kind	Eq. (2.6)	

Greek

$\alpha$	incidence angle of line of sight from transmitter	Eq. (1.1)	Fig. 1.1
$\beta$	general scattering angle	Eq. (2.19)	
$\beta_1$	scattering angle of first-order grating lobe	Eq. (1.1)	Fig. 1.1
$\beta_{3dB}$	3 dB beamwidth in angle	Eq. (2.49)	
$\Gamma$	central angle between users	Eq. (4.10)	
$\gamma$	bistatic scattering angle (also $\theta$ )	Eq. (4.9)	
$\gamma_k$	polar angle to kth element	Eq. (3.37)	Fig. 3.3
$\Delta\beta$	angular departure from center of first-order grating lobe	Eq. (2.43)	
$\Delta\beta_{3dB}$	3 dB angular departure from center of first-order grating lobe	Eq. (2.49)	
$\Delta\lambda$	wavelength departure from center of first-order grating lobe	Eq. (2.51)	
$\Delta\lambda_{3dB}$	3 dB wavelength departure from center of first-order grating lobe	Eq. (2.56)	
$\Delta f$	frequency departure from center of first-order grating lobe	Eq. (2.57)	
$\Delta f_{3dB}$	3 dB frequency departure from center of first-order grating lobe	Eq. (2.58)	

$\delta_k$	supplementary scattering angle to kth element	Eq. (3.20)	Fig. 3.3
$\epsilon$	nadir angle of line of sight	Eq. (3.19)	Fig. 3.3
$\zeta$	angle between line of sight and plane of flexure	Eq. (3.43)	Fig. 3.5
$\eta$	antenna aperture efficiency	Eq. (4.24)	
$\theta_P$	longitude of earth point (user)	Eq. (4.4)	Fig. 4.1
$\theta_S$	longitude of satellite	Eq. (4.4)	Fig. 4.1
$\dot{\theta}_S$	relative orbital angular rate of satellite	Eq. (4.3)	
$\theta$	bistatic scattering angle (also $\gamma$ )	Eq. (2.3)	Fig. 2.1
$\theta$	polar angle to earth reference point	Eq. (3.18)	Fig. 3.3
$\theta_{\max}$	maximum polar angle (to edge of coverage area)	Eq. (3.17)	
$\lambda$	operating wavelength	Eq. (1.1)	
$\lambda_k$	meridional angle to kth element	Eq. (3.22)	Fig. 3.3
$\lambda_0$	wavelength for end-fire array backscattering	Eq. (2.40)	
$\lambda_1$	wavelength to direct first-order grating lobe toward receiver	Eq. (2.26)	
$\mu$	earth's gravitational constant ( $1.4076 \times 10^{16} \text{ ft}^3/\text{sec}^2$ )	Eq. (4.1)	
$\mu_k$	polar angle to kth element	Eq. (3.22)	Fig. 3.3
$\nu$	meridional angle to array axis	Eq. (3.22)	Fig. 3.3
$\phi_P$	latitude of earth point (user)	Eq. (4.4)	Fig. 4.1
$\phi$	meridional angle to earth reference point	Eq. (3.22)	Fig. 3.3
$\sigma_{xy}$	scattering cross section, y to x polarization	Eq. (2.17)	
$\psi$	libration (tilt) angle of array	Eq. (3.23)	Fig. 3.3
$\Omega$	rotational rate of the earth ( $7.2921 \times 10^{-5} \text{ rad/sec}$ )	Eq. (4.3)	Fig. 4.1
$\omega$	meridional angle of array plane	Eq. (3.23)	Fig. 3.3
$\omega$	orbital rate of satellite	Eq. (4.1)	Fig. 4.1
$\omega_0$	carrier frequency	Eq. (2.1)	

## I. SYNOPSIS

The survivability and endurance of the communication systems used for the command and control of strategic forces are vital issues. Concern that existing systems may be vulnerable, despite their diversity and specialized design, has led to numerous suggestions for their improvement. Among these is a proposal by Yater [1] for an advanced passive communication satellite. If it proves practicable, this design, now called PACSAT, may be useful for the command and control of strategic forces because it can provide survivable point-to-point communication at low to moderate data rates between moderate sized mobile terminals within a few thousand miles of one another.

A typical PACSAT communication link is illustrated in Fig. 1.1. PACSAT consists of a uniform linear array of scatterers whose axis is pointed (ideally) toward the center of the earth; gravity-gradient stabilization is used to keep the array erect. When illuminated by a transmitter on the earth, the array scatters energy much like a diffraction grating. The element spacing is chosen such that only the first two grating lobes are generated. Because of the length and the radial symmetry of the array, these grating lobes are in the form of thin-walled cones. The zeroth-order grating lobe is directed out to space at a half angle  $\alpha$  equal to that between the line of sight from the transmitter to the array and the array axis. The first-order grating lobe is directed back toward the earth at a half angle  $\beta_1$ , which is governed by the relationship

$$s(\cos \alpha + \cos \beta_1) = \lambda \quad (1.1)$$

where  $s$  is the element spacing and  $\lambda$  is the operating wavelength. Inasmuch as  $\lambda$  or, equivalently, the frequency  $f$  can be chosen to give  $\beta_1$  any desired value, the scattered beam is said to be frequency-steerable.

To establish a communication link using PACSAT, an operating wavelength is chosen such that the annulus illuminated on the earth by the

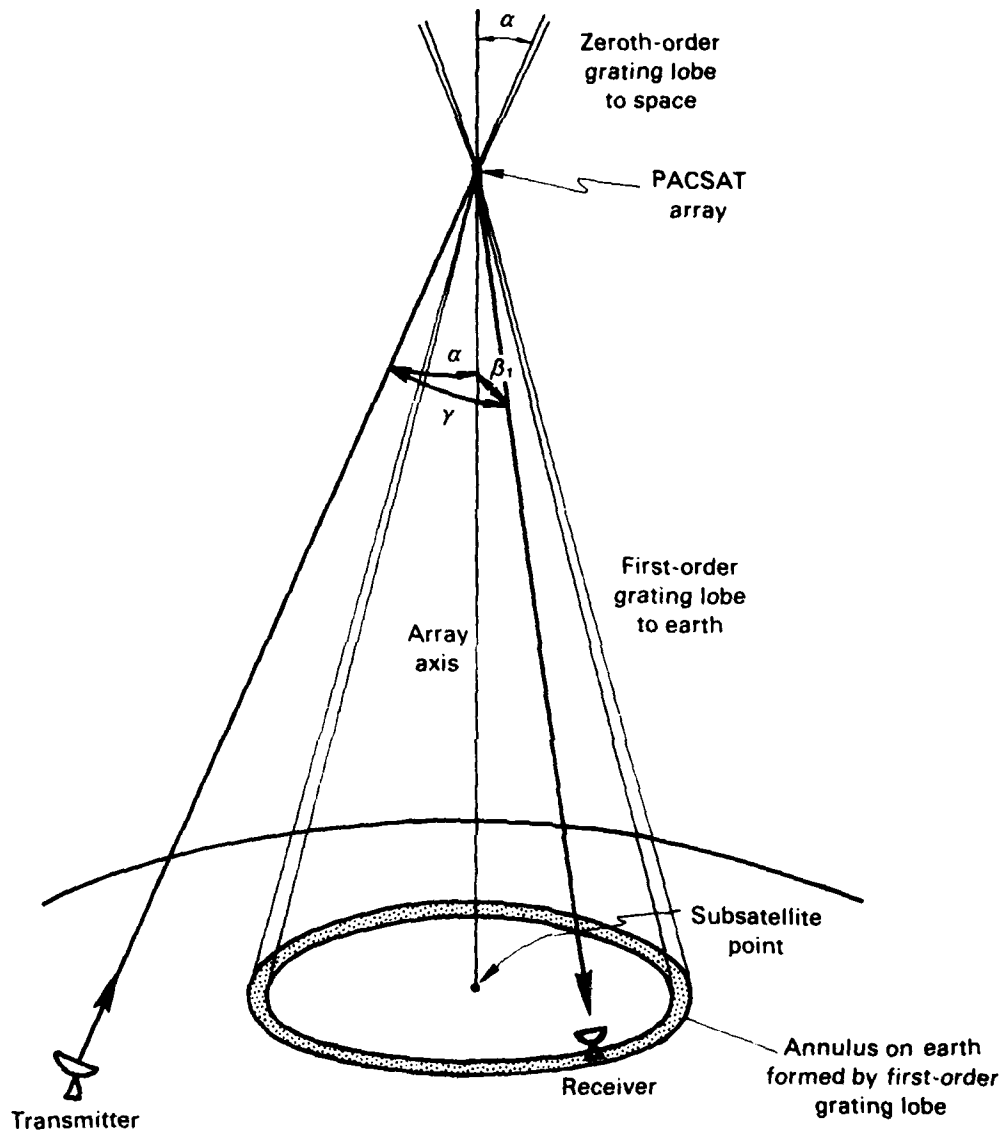


Fig. 1.1 — The PACSAT communication link

first-order grating lobe includes the desired receiver. Except for slight Doppler effects, this operating wavelength would also cause the receiver to illuminate the transmitter were their locations reversed. Also illustrated on Fig. 1.1 is the bistatic scattering angle  $\gamma$  between

the two lines of sight. When discussed in connection with scattering theory this angle will be denoted by  $\theta$ .

The basic command and control communication problem and a general description of the PACSAT concept are presented in a companion Note [2], which serves as a comprehensive introduction to this report. The companion Note can profitably be read first to establish the context for PACSAT and to gain a simple understanding of its basic technical properties and its system characteristics in a practical application. Here, the electromagnetic properties and communication characteristics on which that Note draws are presented in detail. The present report is purely technical and is intended only to provide basic design information and general system characteristics. Issues such as cost, jam resistance, physical survivability, erection techniques, replenishment and augmentation strategies, and flexural dynamics will be treated in forthcoming publications.

The electromagnetic properties of the PACSAT array in the far field are treated in Sec. II. The known Mie solution [3] for scattering from a sphere is reviewed and adapted for the case of circularly polarized illumination and scattering, which is the one of practical interest. The gain of the array in the far field is then calculated assuming uniform illumination along the array (that is, end effects are disregarded). These results are combined to arrive at the far-field scattering cross section of the array, assuming that mutual effects between scatterers can be ignored. The section concludes with a computation of the directivity pattern of the array in the far field.

Defocusing caused by array flexure and near-field operation are examined in Sec. III. It is assumed that the effect can be represented adequately by the leading nonlinear term in the expansion of the general path length expression. This quadratic term is then used to define a defocusing parameter that completely characterizes the effect of array flexure and near-field operation on the array scattering cross section and directivity pattern. The specific geometry of PACSAT in orbit is then used to relate the defocusing parameter to practical array and system parameters. Results are presented in the

form of a tradeoff between allowable array flexure and length for an acceptable amount of defocusing as a function of orbital altitude and array libration for typical user locations. Adequate scattering cross sections ( $0.5$  to  $1.0 \times 10^6 \text{ m}^2$ ) can be realized if: (1) the orbital altitude is no less than 8000 km or so; (2) the libration is limited to 2 or 3 deg at most; and (3) the flexure does not exceed an eighth of a wavelength or so. The last condition is particularly stringent because a typical operating wavelength may be only 3.75 cm (8 GHz).

The system implications of using PACSAT in a circular equatorial orbit are considered in Sec. IV. As noted in the companion Note, this orbit is particularly desirable because it not only limits the required beam-steering frequency excursions and facilitates satellite acquisition and tracking, but also provides adequate CONUS coverage. The geometrical and orbital properties are investigated to show how the orbital period, relative angular rate, and coverage are related to orbital altitude. Satellite azimuth and elevation angle trajectories, orbital arcs of mutual visibility, and mutual viewing times are calculated for typical user locations. The second and third of these show that satellite spacings of about 60 deg and mutual viewing times of about 60 min can be achieved only by the use of orbital altitudes of 8000 km or so. Next, some major array operating parameters are calculated. These include the bistatic scattering angle and the extremes of operating wavelength that would be experienced by typical users as a function of orbital altitude. The first of these is needed to calculate the scattering cross section and the second to set the libration allowable if the frequency excursions are to be accommodated within existing frequency allocations. The latter leads, typically, to a libration limit of a few degrees at most.

Representative optimal array design parameters are then calculated and it is seen that the achievable scattering cross section ranges from about  $0.55L^2$  at orbital altitudes of 4000 to 5000 km to about  $0.65L^2$  at 10,000 km (these results are given in terms of the array length  $L$ ). Finally, some typical communication characteristics are presented in the form of power budgets. These indicate that PACSAT may be useful for low data rate communication between mobile or transportable

terminals. For example, a 1 kbps data rate can be supported between 1 m diameter dishes at a frequency of 8 GHz using a 10 kW transmitter, a low-noise receiver, and a PACSAT array with a scattering cross section of  $10^6 \text{ m}^2$  (about 1300 m long) at an orbital altitude of 6000 km.

## II. ELECTROMAGNETIC PROPERTIES IN THE FAR FIELD

The field scattered back to the earth by the PACSAT array at a great distance is investigated in this section. It is assumed that PACSAT consists of a uniform linear array of perfectly conducting spheres whose axis is pointed (ideally) toward the center of the earth. First, the known far-field scattering properties of a single sphere are reviewed and its scattering cross section for circularly polarized illumination and scattering is calculated over the range of bistatic scattering angles and sphere sizes of interest. Then, the gain of the array in the far field is derived and used to calculate the bistatic far-field scattering cross section of the array. Finally, its directivity pattern and beam characteristics in the far field are developed.

### FAR-FIELD SCATTERING FROM A SPHERE

The problem of scattering from a sphere was solved exactly by Mie [3] in 1908 and is discussed in Stratton [4]; the results presented here are from Barrick [5].

Consider an incident plan wave

$$\vec{E}_x^i = E_x^i e^{-i(k_0 z + \omega_0 t)} \vec{x} \quad (2.1)$$

where  $\vec{x}$  is a unit vector in the x direction,

$$k_0 = \frac{2\pi}{\lambda} \quad (2.2)$$

and  $\lambda$  is the wavelength; the harmonic time dependence will be suppressed henceforth. As illustrated in Fig. 2.1, the incident field is linearly polarized in the x-z or E-plane and is propagating in the -z direction. A sphere of radius a is at the origin and the scattered field is desired at a point at a distance r, polar angle  $\theta$ , and



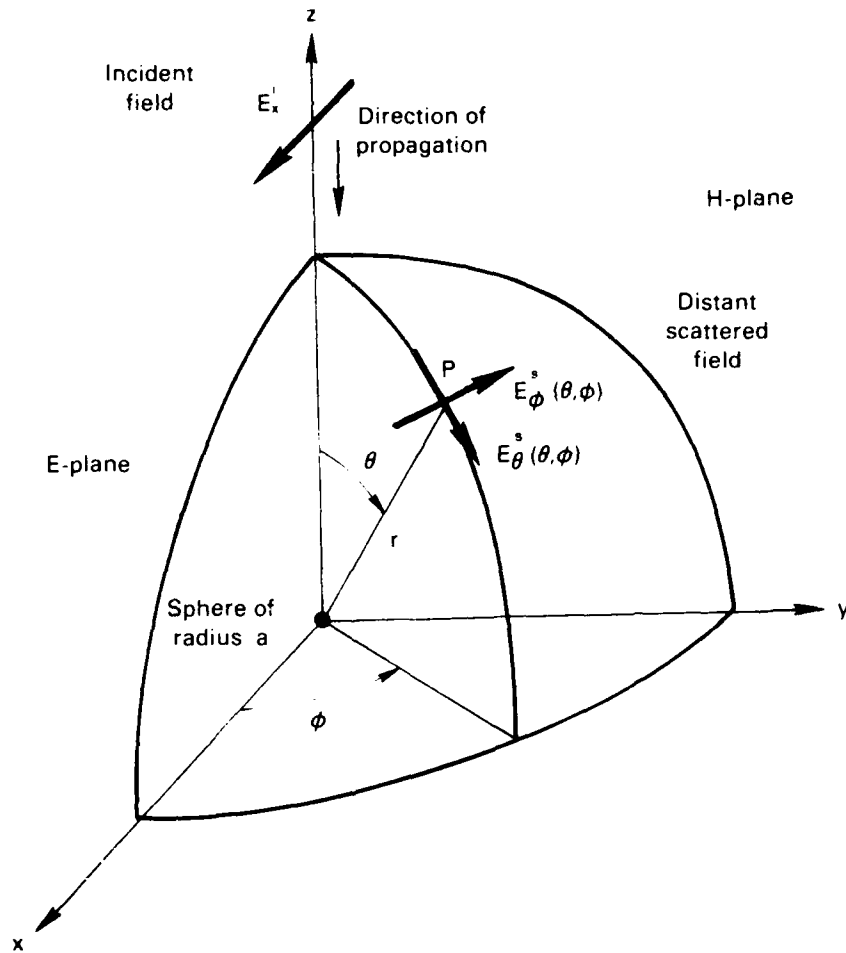


Fig. 2.1 — Geometry of field scattered from a sphere

meridional angle  $\phi$ , with respect to the  $x$ - $z$  plane. The angle  $\theta$  is also known as the bistatic scattering angle; in the monostatic case,  $\theta = 0$  and the field is said to be backscattered.\*

\*The bistatic scattering angle is denoted by  $\theta$  in this section to conform with standard usage in scattering theory. Inasmuch as  $\theta$  is also conventionally used to denote the polar angle in spherical geometry, it is used for that purpose elsewhere in this report and  $\gamma$  is then used to denote the bistatic scattering angle.

When the distance is great, the scattered field is essentially a spherical wave that can be expressed as

$$\bar{E}_x^s(\theta, \phi) = E_x^i \frac{e^{ik_0 r}}{k_0 r} \left[ S_1(\theta) \cos \phi \bar{\theta} - S_2(\theta) \sin \phi \bar{\phi} \right] \quad (2.3)$$

The functions  $S_1$  and  $S_2$  are given by

$$S_1(\theta) = \sum_{n=1}^{\infty} (-1)^{n+1} \left[ A_n \frac{P_n^1(\cos \theta)}{\sin \theta} + i B_n \frac{d}{d\theta} P_n^1(\cos \theta) \right] \quad (2.4)$$

$$S_2(\theta) = \sum_{n=1}^{\infty} (-1)^{n+1} \left[ A_n \frac{d}{d\theta} P_n^1(\cos \theta) + i B_n \frac{P_n^1(\cos \theta)}{\sin \theta} \right]$$

where  $P_n^1$  is the associated Legendre function. For a perfectly conducting sphere of radius  $a$ , the coefficients  $A_n$  and  $B_n$  are given by

$$A_n = -(-1)^n \frac{2n+1}{n(n+1)} \frac{j_n(k_0 a)}{h_n^{(1)}(k_0 a)} \quad (2.5)$$

$$B_n = (-1)^{n+1} \frac{2n+1}{n(n+1)} \frac{\left[ k_0 a j_n(k_0 a) \right]'}{\left[ k_0 a h_n^{(1)}(k_0 a) \right]'}$$

where the prime denotes differentiation with respect to  $k_0 a$  and

$$h_n^{(1)}(z) = j_n(z) + i y_n(z) \quad (2.6)$$

is the spherical Bessel function of the third kind.

The  $\theta$  and  $\phi$  components of the scattered field are depicted in Fig. 2.1. It is apparent from Eq. (2.3) that there is only a  $\theta$  component in the E-plane ( $\phi = 0$ ) and only a  $\phi$  component in the H-plane ( $\phi = \pi/2$ ); thus, the scattered field is linearly polarized in these planes. Elsewhere, because these components are complex and unequal, in general, the scattered field is elliptically polarized (though only weakly so for the range of values of  $k_0 a$  and  $\theta$  of interest).

A more general representation in which the incident linearly polarized field has an arbitrary orientation can be obtained by considering a second incident field that is linearly polarized in the  $y$  direction. Thus, for

$$\bar{E}_y^i = E_y^i e^{-ik_0 z} \quad (2.7)$$

the scattered field can be written by substituting  $\phi = \pi/2$  for  $\phi$  in Eq. (2.3) to obtain

$$\bar{E}_y^s(\theta, \phi) = E_y^i \frac{e^{ik_0 r}}{k_0 r} \left[ S_1(\theta) \sin \phi \bar{\theta} + S_2(\theta) \cos \phi \bar{\phi} \right] \quad (2.8)$$

The arbitrarily oriented, linearly polarized, incident plane wave is then equal to the sum of Eqs. (2.1) and (2.7), or

$$\bar{E}^i = \bar{E}_x^i + \bar{E}_y^i \quad (2.9)$$

and the general total scattered field is given by the sum of Eqs. (2.3) and (2.8), or

$$\begin{aligned}\bar{E}^s(\theta, \phi) &= E_{\theta}^s(\theta, \phi) \bar{\theta} + E_{\phi}^s(\theta, \phi) \bar{\phi} \\ &= \frac{ik_0 r}{k_0 r} \left[ S_1(\theta) (E_x^i \cos \phi + E_y^i \sin \phi) \bar{\phi} \right. \\ &\quad \left. + S_2(\theta) (-E_x^i \sin \phi + E_y^i \cos \phi) \bar{\theta} \right] \quad (2.10)\end{aligned}$$

In matrix form, this becomes

$$\begin{bmatrix} E_{\theta}^s(\theta, \phi) \\ E_{\phi}^s(\theta, \phi) \end{bmatrix} = \begin{bmatrix} a_{\theta x} & a_{\theta y} \\ a_{\phi x} & a_{\phi y} \end{bmatrix} \begin{bmatrix} E_x^i \\ E_y^i \end{bmatrix} \quad (2.11)$$

where

$$\begin{aligned}a_{\theta x} &= \frac{ik_0 r}{k_0 r} S_1(\theta) \cos \phi, & a_{\theta y} &= \frac{ik_0 r}{k_0 r} S_1(\theta) \sin \phi \\ a_{\phi x} &= -\frac{ik_0 r}{k_0 r} S_2(\theta) \sin \phi, & a_{\phi y} &= \frac{ik_0 r}{k_0 r} S_2(\theta) \cos \phi\end{aligned} \quad (2.12)$$

The double subscript notation on the coefficients of the scattering matrix refers to the polarization of the scattered and incident field components, in that order.

In the PACSAT application, it is desirable to use circular rather than linear polarization for both transmission and reception because it eliminates the need for polarization alignment. The representation of the scattered field in terms of right- and left-hand circularly polarized components when the incident field has both right- and left-hand circularly polarized components can be written in matrix form in a fashion analogous to Eq. (2.11), or

$$\begin{bmatrix} E_R^s(\theta, \phi) \\ E_L^s(\theta, \phi) \end{bmatrix} = \begin{bmatrix} a_{RR} & a_{RL} \\ a_{LR} & a_{LL} \end{bmatrix} \begin{bmatrix} E_R^i \\ E_L^i \end{bmatrix} \quad (2.13)$$

The relationships between the elements of the circular and linear polarization matrices are given by Barrick (Ref. 5, Eqs. (2.1-25)) as

$$a_{RR} = 1/2 \left[ (-a_{\phi y} + a_{\theta x}) - i(a_{\theta y} + a_{\phi x}) \right], \quad a_{RL} = 1/2 \left[ (a_{\phi y} + a_{\theta x}) + i(a_{\theta y} - a_{\phi x}) \right] \quad (2.14)$$

$$a_{LR} = 1/2 \left[ (a_{\phi y} + a_{\theta x}) - i(a_{\theta y} - a_{\phi x}) \right], \quad a_{LL} = 1/2 \left[ (-a_{\phi y} + a_{\theta x}) + i(a_{\theta y} + a_{\phi x}) \right]$$

Substituting Eqs. (2.12) in Eqs. (2.14) then yields

$$a_{RR} = \frac{e^{ik_0 r}}{2k_0 r} \left\{ \left[ S_1(\theta) - S_2(\theta) \right] \cos \phi - i \left[ S_1(\theta) - S_2(\theta) \right] \sin \phi \right\} \quad (2.15)$$

$$a_{LR} = \frac{e^{ik_0 r}}{2k_0 r} \left\{ \left[ S_1(\theta) + S_2(\theta) \right] \cos \phi - i \left[ S_1(\theta) + S_2(\theta) \right] \sin \phi \right\}$$

It can be seen from Eqs. (2.14) that the other coefficients are given by

$$a_{LL} = a_{RR} e^{i2\phi}, \quad a_{RL} = a_{LR} e^{i2\phi} \quad (2.16)$$

Finally, the various scattering cross sections are given by

$$\begin{aligned}\sigma_{RR} &= 4\pi r^2 |a_{RR}|^2, & \sigma_{LR} &= 4\pi r^2 |a_{LR}|^2 \\ \sigma_{RL} &= 4\pi r^2 |a_{RL}|^2, & \sigma_{LL} &= 4\pi r^2 |a_{LL}|^2\end{aligned}\tag{2.17}$$

so substituting from Eqs. (2.15) and (2.16) yields

$$\begin{aligned}\sigma_{RR} = \sigma_{LL} &= \frac{\pi}{k_0^2} \left\{ \left[ \text{Re } S_1(\theta) - \text{Re } S_2(\theta) \right]^2 + \left[ \text{Im } S_1(\theta) - \text{Im } S_2(\theta) \right]^2 \right\} \\ \sigma_{LR} = \sigma_{RL} &= \frac{\pi}{k_0^2} \left\{ \left[ \text{Re } S_1(\theta) + \text{Re } S_2(\theta) \right]^2 + \left[ \text{Im } S_1(\theta) + \text{Im } S_2(\theta) \right]^2 \right\}\end{aligned}\tag{2.18}$$

where Re and Im denote the real and imaginary parts, respectively.

For the PACSAT application, the bistatic scattering angle  $\theta$  will generally be less than about 45 deg or so. Furthermore, to maximize the field scattered toward the receiver, it is desirable to operate in the vicinity of the first resonance, which occurs at values of  $k_0a$  of about 1.0 to 1.1. (It will be seen later that the peak of the resonance for the array of spheres shifts the values of  $k_0a$  to about 1.1 to 1.2.) Therefore, the scattering cross sections have been evaluated numerically for  $k_0a$  values of between 0.9 and 1.4 and values of  $\theta$  from 0 to 50 deg. The same-sense scattering cross section  $\sigma_{RR}$  or  $\sigma_{LL}$  is small and of no practical interest. The opposite-sense scattering cross section  $\sigma_{LR}$  or  $\sigma_{RL}$ , which conveys virtually all of the scattered energy, is plotted in Fig. 2.2 after normalization to its physical cross section  $\pi a^2$ . (See the appendix for details of the computation.)

To facilitate reading the three-dimensional plot, contours of constant  $\sigma_{LR}/\pi a^2$  are shown as solid lines on the surface. Also shown, as dashed lines, are contours of constant  $\theta$  and  $k_0a$ . A heavy dashed line indicates the ridge along which the function takes on a local maximum. As mentioned earlier, the contour for  $\theta = 0$  is the

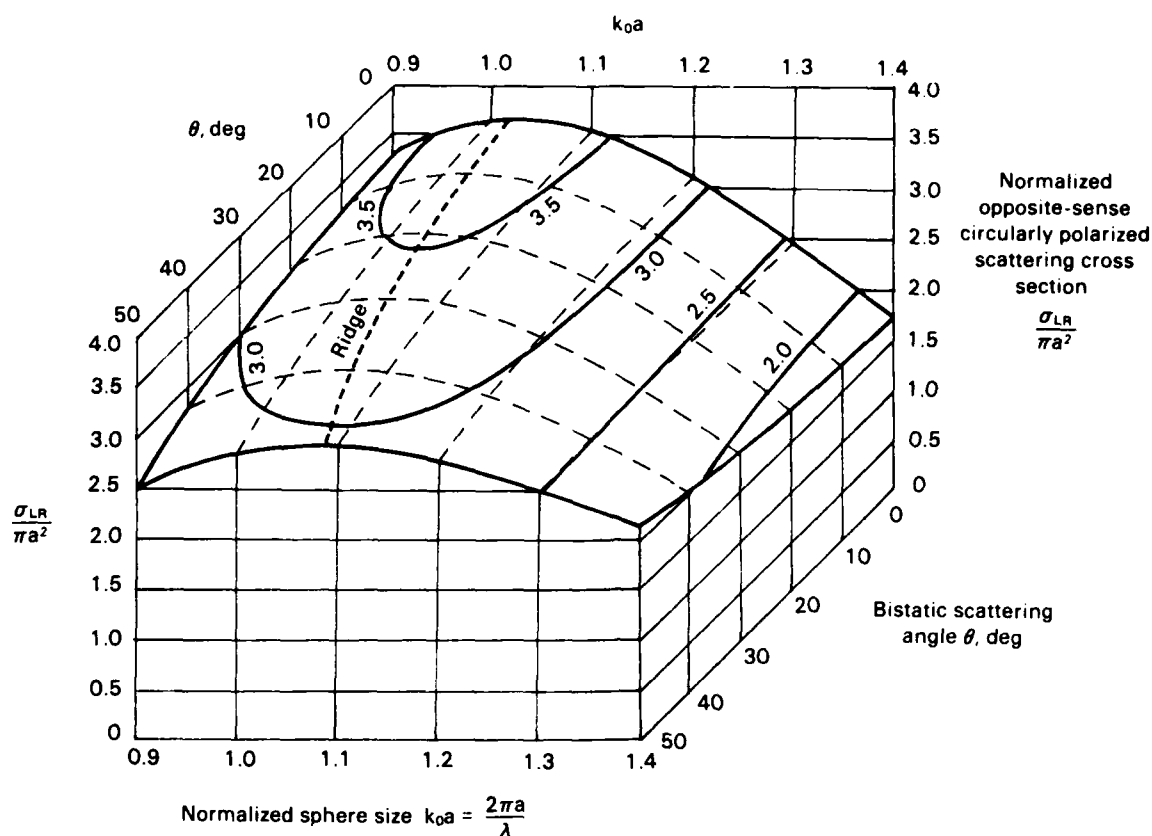


Fig. 2.2 — Scattering from a sphere of radius  $a$  at wavelength  $\lambda$

back-scattering case for which the familiar plot is shown in Fig. 2.3. (There is no difference between the appropriately sensed linear and circular polarization combinations for back scattering.) The portion shown in Fig. 2.2 is thus seen to be in the vicinity of the first (and largest) resonance in Fig. 2.3 at which the back-scattering cross section is slightly more than 3.6 times the physical cross section. It might be noted that this resonance occurs when the circumference of the sphere is slightly more than one wavelength.

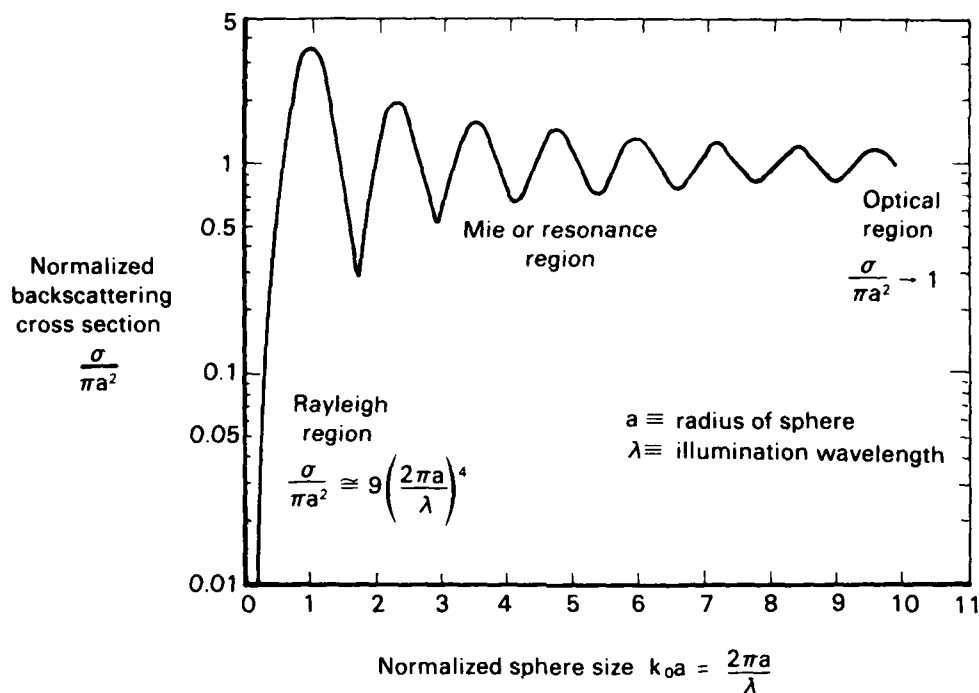


Fig. 2.3 — The normalized radar or backscattering cross section of a perfectly conducting sphere

#### GAIN OF THE ARRAY IN THE FAR FIELD

The far-field geometry of the PACSAT array is shown in Fig. 2.4. The  $N$  scattering elements, which are assumed to be isotropic, are spaced a uniform distance  $s$  along the array axis. When the array is illuminated from a great distance at an angle  $\alpha$  with respect to its axis, the incoming rays can be considered parallel. The rays representing the scattering toward a distant point at an angle  $\beta$  can then also be considered parallel. It is clear, from symmetry, that the planes containing the incident and scattered rays need not be coincident, i.e., there is axial symmetry.

The uniform element spacing results in a uniform path lengthening or phase progression between successive rays. It will be assumed that the elements are uniformly illuminated, which is equivalent to ignoring end effects. It is well known that the currents induced on passive array elements are influenced by the presence of other nearby elements. When the array symmetry is appropriate, as when the elements



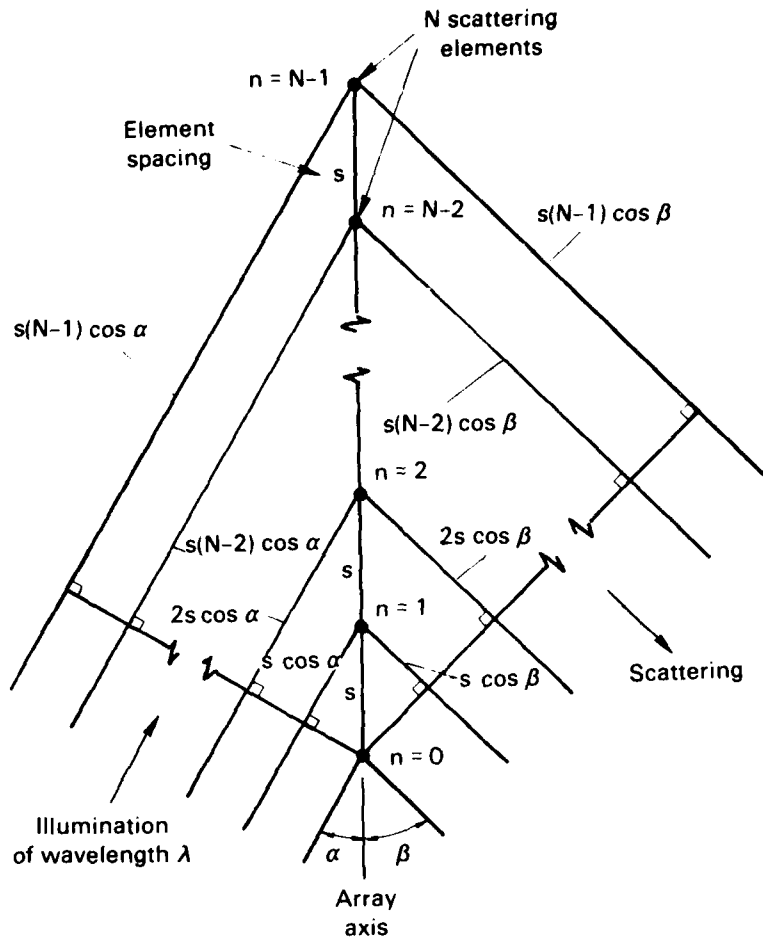


Fig. 2.4 — The basic PACSAT array

are in a ring, these mutual effects will be the same for all elements and there is no approximation. If there are a large number of elements in non-symmetrical configurations, as would be the case for PACSAT, only the elements near the ends of the array would experience significantly different mutual effects. This end effect is considered negligible for PACSAT and will be ignored.

The magnitude of the scattered field can be written

$$|E| = \left| \sum_{n=0}^{N-1} \exp i \frac{2\pi}{\lambda} ns(\cos \alpha + \cos \beta) \right| \quad (2.19)$$

where the individual elements are assumed to contribute unit amplitudes at the receiving point. The sum can be expressed in closed form as

$$|E| = \frac{\sin \frac{1}{2}Nx}{\sin \frac{1}{2}x} \quad (2.20)$$

where

$$x = 2\pi \frac{s}{\lambda} (\cos \alpha + \cos \beta) \quad (2.21)$$

Inasmuch as the spacing  $s$  and the illumination angle  $\alpha$  are parameters of the problem, the amplitude of the scattered field is a function of two variables: the scattering angle  $\beta$  and the wavelength  $\lambda$ . Also, the scattered field has maxima, of amplitude  $N$ , called grating lobes, whenever

$$\frac{s}{\lambda} (\cos \alpha + \cos \beta) = k, \quad k = 0, 1, 2, \dots \quad (2.22)$$

where  $k$  is the order of the grating lobe.

The zeroth-order grating lobe ( $k = 0$ ) occurs when

$$\beta = \pi - \alpha \quad (2.23)$$

so it is independent of  $\lambda$ ; it is shown in Fig. 1.1 as the grating lobe scattering off into space (for practical values of  $\alpha$ ). The first-order grating lobe ( $k = 1$ ) occurs when  $\beta$  and  $\lambda$  satisfy

$$s(\cos \alpha + \cos \beta) = \lambda \quad (2.24)$$

(Grating lobes of higher order are suppressed in the PACSAT application by avoiding values of  $\lambda$  small enough to satisfy Eq. (2.22) for  $k > 2$ .) It is convenient to specify the center of the first-order grating lobe given by Eq. (2.24) by either fixing  $\lambda$  and letting  $\beta = \beta_1$  denote the angle at which it occurs, i.e.,

$$s(\cos \alpha + \cos \beta_1) = \lambda \quad (2.25)$$

or fixing  $\beta$  and letting  $\lambda = \lambda_1$  denote the wavelength at which it occurs, i.e.,

$$s(\cos \alpha + \cos \beta) = \lambda_1 \quad (2.26)$$

The first of these is used in Eq. (1.1) and in Fig. 1.1 to depict the frequency-steerable first-order grating used to form a communication link. It will also be used in this subsection to integrate the scattered field over  $\beta$ . Both will be used later to describe the directivity pattern in the vicinity of the main lobe.

The gain of the array is defined as the ratio of the field intensity in the direction of maximum radiation to the average intensity of radiation in all directions. Thus,

$$G = \frac{|E|_{\max}^2}{\frac{1}{4} \pi \int |E|^2 d\Omega} \quad (2.27)$$

where the integral is over the sphere. It is apparent from Eq. (2.20) that

$$|E|_{\max}^2 = N^2 \quad (2.28)$$

To facilitate the integration on  $\beta$ , use Eq. (2.25) to eliminate  $\lambda$  in Eq. (2.21). Then, using

$$x = 2\pi \frac{\cos \alpha + \cos \beta}{\cos \alpha + \cos \beta_1} \quad (2.29)$$

as a change of variables in Eq. (2.20), and conventional spherical variables, the integral in the denominator of Eq. (2.27) becomes

$$\begin{aligned} \mathcal{J} &= \int_0^{2\pi} d\phi \int_0^{\pi} d\beta \frac{\sin^2 \frac{1}{2}Nx}{\sin^2 \frac{1}{2}x} \sin \beta \\ &= (\cos \alpha + \cos \beta_1) \int_v^u \frac{\sin^2 \frac{1}{2}Nx}{\sin^2 \frac{1}{2}x} dx \end{aligned} \quad (2.30)$$

where

$$u = 2\pi \frac{\cos \alpha + 1}{\cos \alpha + \cos \beta_1}, \quad v = 2\pi \frac{\cos \alpha - 1}{\cos \alpha + \cos \beta_1} \quad (2.31)$$

The integrand of Eq. (2.30) is plotted in Fig. 2.5 for  $N = 12$  and  $17$  and  $\alpha = \beta_1 = 30$  deg to illustrate its behavior (the abscissa is linear in  $x$ ). The function attains its maximum value of  $N^2$  at  $x = 0, 2\pi$ , which correspond to the values of  $\beta$  for the zeroth- and first-order grating lobes, respectively. Even for small numbers of elements in the array, the principal contribution to the integral is seen to be in the vicinity of these values of  $x$ . As  $N$  increases, the peak value increases rapidly and the integrand goes through an increasing number of oscillations (these are actually the sidelobes of the array pattern in the angle  $\beta$ ). Also, the integrand compacts about the values at which it attains its peak value. Inasmuch as practical values of  $N$  will be in the tens of thousands, it is clear that the integral can be well approximated by writing it as the sum of two overlapping infinite integrals in which the sine function in the denominator is expanded about  $x = 0, 2\pi$ . Thus Eq. (2.30) can be written

$$\mathcal{J} = \cos \alpha + \cos \beta_1 \int_v^{\infty} \frac{\sin^2 \frac{1}{2}Nx}{(\frac{1}{2}x)^2} dx + \int_{-\infty}^u \frac{\sin^2 \frac{1}{2}Nx}{[\frac{1}{2}(x - 2\pi)]^2} dx \quad (2.32)$$

The limits  $u$  and  $v$  have been retained in Eq. (2.32) to accommodate the cases when  $v$  is near  $0$  and  $u$  is near  $2\pi$ , which correspond to  $\alpha$  and  $\beta_1$  small, respectively.

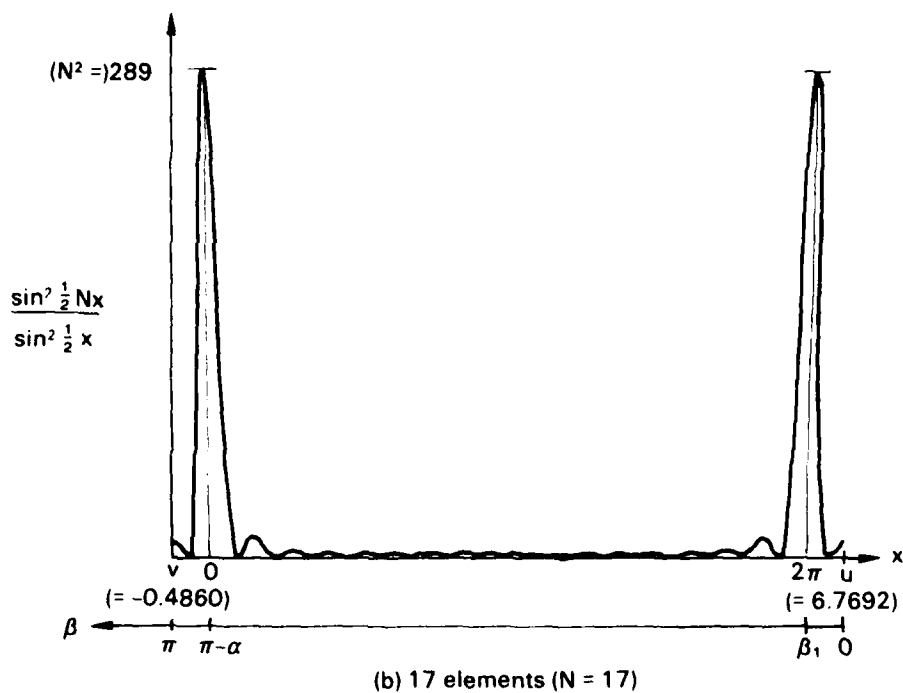
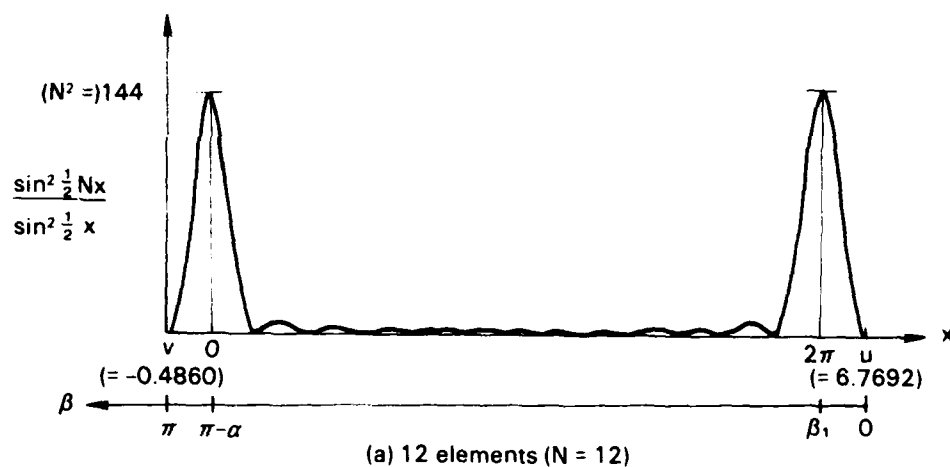


Fig. 2.5 — Plots of integrand of Eq. (2.32) for  $\alpha = \beta_1 = \pi/6$

The integrals in Eq. (2.32) are easily evaluated and, when substituted in Eq. (2.27), yield

$$G = \frac{2\pi N}{(\cos \alpha + \cos \beta_1) \left[ \pi + \text{Si } N(u - 2\pi) - \frac{1 - \cos N(u - 2\pi)}{N(u - 2\pi)} - \text{Si } Nv + \frac{1 - \cos Nv}{Nv} \right]} \quad (2.33)$$

where  $\text{Si}$  is the sine integral. Limiting cases occur when: (1) both  $\alpha$  and  $\beta_1$  are equal to zero; (2) when either  $\alpha$  or  $\beta_1$  is equal to zero and the other is sufficiently large that its associated integral in Eq. (2.32) takes on its value for infinite limits; and (3) when both  $\alpha$  and  $\beta_1$  are similarly sufficiently large. To establish such a criterion for  $\alpha$  and  $\beta_1$ , recall that the principal contribution to the integrals in Eq. (2.32) comes from the main lobe of the integrand. It can be shown that if the integration is to the first null, the integral attains 95 percent of its final value; if the integration is to the fifth null, the integral reaches 99 percent of its final value. Thus, if  $\alpha$  (or  $\beta_1$ ) is not "small," where "small" means on the order of a few beamwidths, its associated integral in Eq. (2.32) essentially takes on the value for  $v = -\infty$  (or  $u = +\infty$ ). The array gain, Eq. (2.33), can then be specialized to the following cases:

$$G = \begin{cases} N, & \alpha = \beta_1 = 0 \\ \frac{\frac{4}{3} N}{1 + \cos \beta_1}, & \alpha = 0, \beta_1 \text{ not small} \\ \frac{\frac{4}{3} N}{1 + \cos \alpha}, & \beta_1 = 0, \alpha \text{ not small} \\ \frac{N}{\cos \alpha + \cos \beta_1}, & \alpha, \beta_1 \text{ not small} \end{cases} \quad (2.34)$$

The cases for either  $\alpha$ ,  $\beta_1$ , or both small or equal to zero, all of which result in end-fire operation of the array, are not of practical interest because they correspond to fleeting or unlikely geometries. Most of the time, the gain will be given by the fourth of Eqs. (2.34). Inasmuch as it is also a conservative value, it will be used in the following analysis.

# FAR-FIELD SCATTERING FROM THE ARRAY

The scattering cross section  $\sigma$  of the array is defined as

$$\sigma = GA_{\text{eff}} \quad (2.35)$$

where  $G$  is the array gain given by Eqs. (2.34) and  $A_{\text{eff}}$  is its effective capture cross section. As noted above, the gain will be taken as the fourth of Eqs. (2.34). It will be assumed that mutual effects between the individual spheres comprised by the array can be ignored so that the effective capture cross section of the array can be taken as  $N$  times the scattering cross section of an isolated sphere, i.e.,

$$A_{\text{eff}} = N\sigma_{\text{LR}} \quad (2.36)$$

where  $\sigma_{\text{LR}}$  is given by Eq. (2.18). The magnitude of the error inherent in the assumption is not known but, unfortunately, an exact analysis does not appear possible so there is no choice. It is hoped, by analogy to the known properties of conventional antenna arrays, that the error is not significant.

Substituting from the fourth of Eqs. (2.34) and using Eq. (2.25) to reintroduce  $\lambda$  leads to

$$\sigma = \frac{N^2 \sigma_{\text{LR}}}{\lambda} \quad (2.37)$$

Using Eq. (2.2), to introduce  $k_0$ , this can be brought into the form

$$\sigma = \left( \frac{N^2 sa}{2} \right) k_0 a \left( \frac{\sigma_{\text{LR}}}{\pi a^2} \right) \quad (2.38)$$

which permits identifying  $N^2 sa/2$  as an appropriate normalization factor. The term  $\sigma_{\text{LR}}/\pi a^2$  is the normalized scattering cross section of a sphere plotted on Fig. 2.2, so the numerical values need only be multiplied by  $k_0 a$  to obtain the values of the normalized array scattering cross section.

Other forms of the normalization factor can be obtained by noting that the array length  $L$  is given by

$$L = (N - 1)s \cong Ns \quad (2.39)$$

Also, from Eq. (2.25), an end-fire operating wavelength  $\lambda_0$  can be identified by setting  $\alpha = \beta_1 = 0$  to get

$$s = \frac{\lambda_0}{2} \quad (2.40)$$

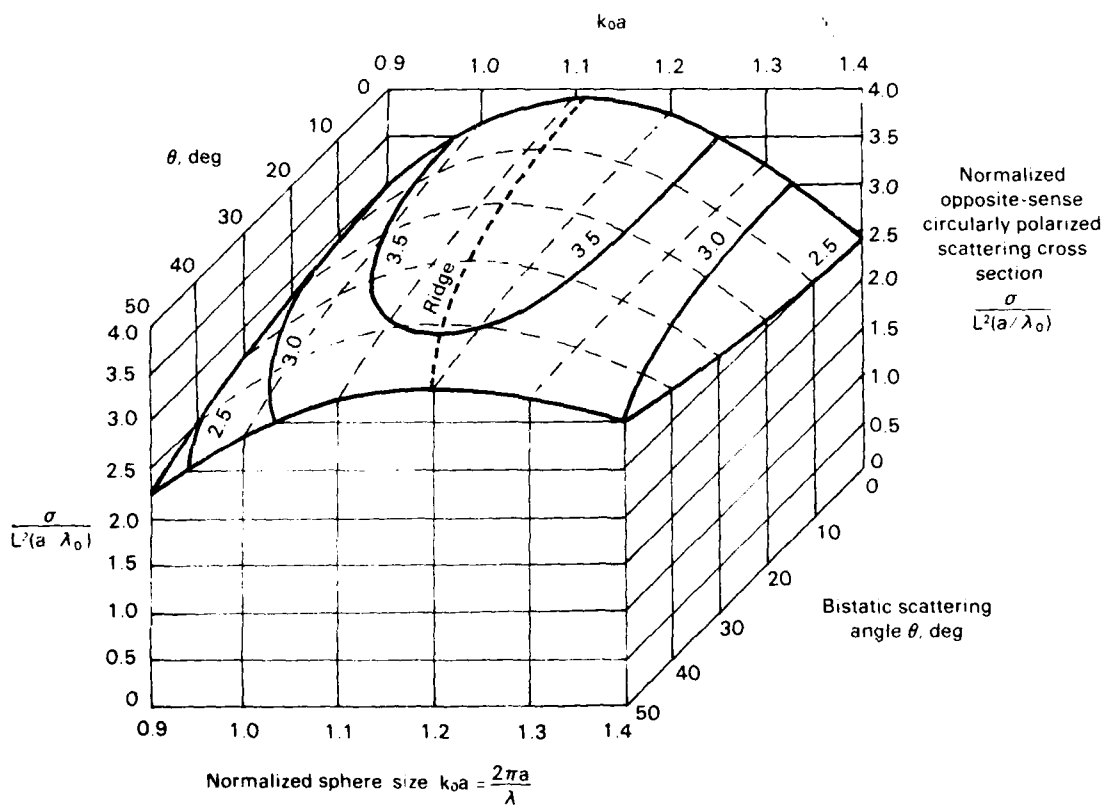


Fig. 2.6 — Scattering from the PACSAT array of length  $L$  at wavelength  $\lambda$



With the help of these, it follows that

$$\frac{N^2 s a}{2} = \frac{L^2 a}{2s} = \frac{L^2 a}{\lambda_0} = \frac{N^2 a \lambda_0}{4} \quad (2.41)$$

These are equivalent and may be interchanged as preference dictates. Using the simplest form, the normalized array scattering cross section  $\sigma \lambda_0 / L^2 a$  is plotted in Fig. 2.6 in a form similar to that used in Fig. 2.2. The value of  $k_0 a$  at which the maximum is attained is plotted in Fig. 2.7 to facilitate selecting the sphere size that optimizes the

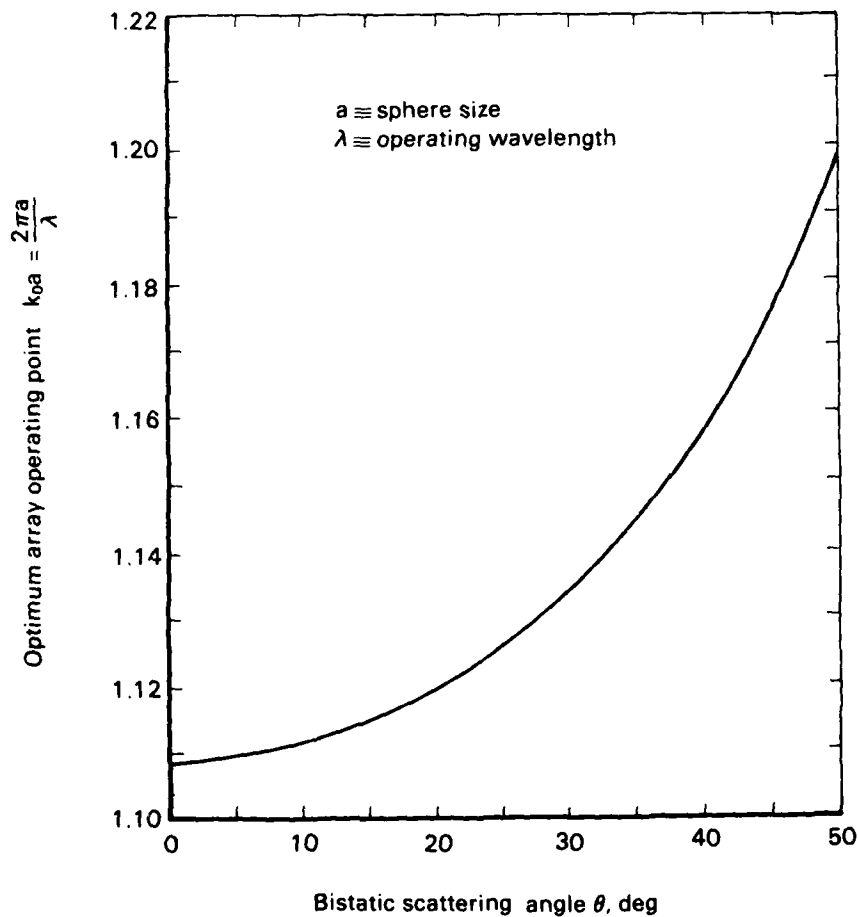


Fig. 2.7 — Optimum scattering from the PACSAT array

design of the array. A practical design procedure will be outlined in the next section and an example shown for PACSAT in a circular equatorial orbit.

#### DIRECTIVITY PATTERN IN THE FAR FIELD

The far-field directivity pattern  $D$  is given by the ratio of the square of Eq. (2.20) to Eq. (2.28) so

$$D = \left( \frac{\sin \frac{1}{2}Nx}{N \sin \frac{1}{2}x} \right)^2 \quad (2.42)$$

where  $x$  is given by Eq. (2.21)

$$x = 2\pi \frac{s}{\lambda} (\cos \alpha + \cos \beta) \quad (2.21)$$

The directivity pattern is desired in the vicinity of the first-order grating lobe. Inasmuch as this grating lobe is a function of both angle and frequency, it is most conveniently expressed by two component directivity patterns. One is the conventional pattern in which the wavelength is fixed and the pattern is expressed in terms of the angular departure from the angle corresponding to the peak of the first-order grating lobe. In the other, the angle is fixed and the pattern is expressed in terms of the wavelength departure from the wavelength corresponding to the peak of the first-order grating lobe.

#### Angle Pattern

For this pattern it is appropriate to use Eq. (2.25) to eliminate  $\lambda$  in Eq. (2.21), so, as above,

$$x = 2\pi \frac{\cos \alpha + \cos \beta}{\cos \alpha + \cos \beta_1} \quad (2.29)$$

Let the angle  $\beta$  be expressed in terms of its departure  $\Delta\beta$  from the beam center  $\beta_1$ , i.e.,

$$\beta = \beta_1 + \Delta\beta \quad (2.43)$$

Then, for  $\Delta\beta$  small

$$\cos \beta = \cos \beta_1 - \Delta\beta \sin \beta_1 \quad (2.44)$$

and

$$\sin \frac{1}{2}Nx = \pm \sin \left( \frac{N\Delta\beta \sin \beta_1}{\cos \alpha + \cos \beta_1} \right) \quad (2.45)$$

where the signum is - for N even and + for N odd. For N = 1 and  $\Delta\beta$  small,

$$\sin \frac{1}{2}x = \frac{\pi\Delta\beta \sin \beta_1}{\cos \alpha + \cos \beta_1} \quad (2.46)$$

so substituting Eqs. (2.45) and (2.46) in Eq. (2.42) yields

$$D = \left( \frac{\sin y}{y} \right)^2 \quad (2.47)$$

where

$$y = \frac{N\pi\Delta\beta \sin \beta_1}{\cos \alpha + \cos \beta_1} \quad (2.48)$$

The 3 dB, or half-power, point occurs when  $y = 1.39156$ , so the 3 dB beamwidth is given by

$$\beta_{3dB} \equiv 2\Delta\beta_{3dB} = 0.8859 \frac{\cos \alpha + \cos \beta_1}{N \sin \beta_1} \quad (2.49)$$

The result is invalid for  $\beta_1$  near zero where the  $\frac{\sin y}{y}$  patterns characterizing the walls of the conical pattern merge into a single  $\frac{\sin y}{y}$  pattern characterizing the end-fire pencil beam.

The near-inverse relationship between the 3 dB beamwidth  $\beta_{3dB}$  and the cone half angle  $\beta_1$  in Eq. (2.49) indicates how the wall thickness of the scattered cone decreases as the cone opens. Note that the total solid angle in the cone is approximately equal to  $2\pi\beta_{3dB} \sin \beta_1$ . Thus, the total solid angle is roughly constant; this is consistent with Eqs. (2.34), which show that the gain is also roughly constant. The normalized 3 dB beamwidth,  $N\beta_{3dB}$ , is plotted as a function of  $\beta_1$  in Fig. 2.8 for a range of illumination angles  $\alpha$ .

#### Wavelength Pattern

For this pattern it is appropriate to use Eq. (2.26) to introduce  $\lambda_1$  in Eq. (2.21) to obtain

$$x = 2\pi \frac{\lambda_1}{\lambda} \quad (2.50)$$

Let the wavelength  $\lambda_1$  be expressed in terms of its departure  $\Delta\lambda$  from the beam-center value  $\lambda_1$ , so

$$\lambda = \lambda_1 + \Delta\lambda \quad (2.51)$$

Then, for  $\Delta\lambda \ll \lambda_1$

$$x = 2\pi \left(1 - \frac{\Delta\lambda}{\lambda_1}\right) \quad (2.52)$$

which leads to

$$\sin \frac{1}{2}Nx = \pm \sin N\pi \frac{\Delta\lambda}{\lambda_1} \quad (2.53)$$

where the signum is - for N even and + for N odd, and

$$\sin \frac{1}{2}x = \pi \frac{\Delta\lambda}{\lambda_1} \quad (2.54)$$

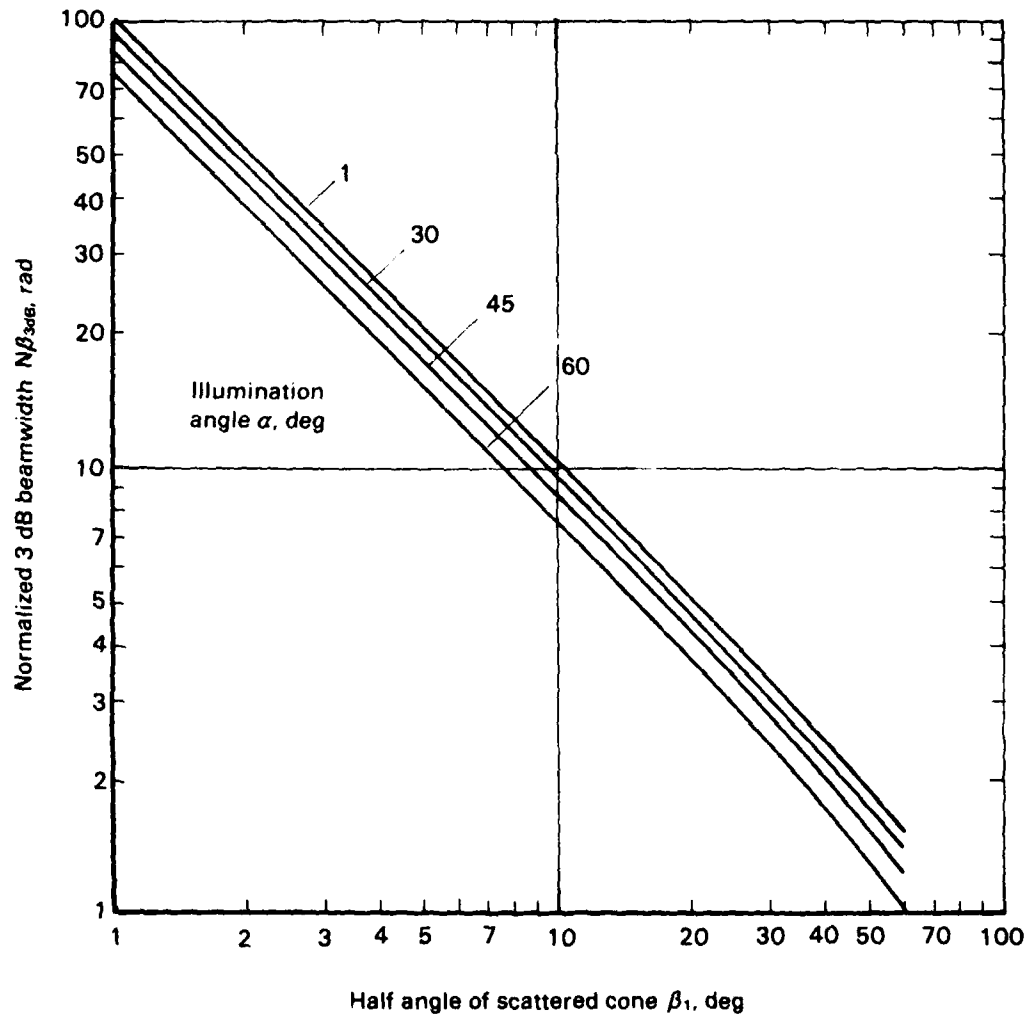


Fig. 2.8 — Normalized 3 dB beamwidth of PACSAT array

Substituting Eqs. (2.53) and (2.54) in Eq. (2.42) then yields

$$D = \left( \frac{\sin N\pi \frac{\Delta\lambda}{\lambda_1}}{N\pi \frac{\Delta\lambda}{\lambda_1}} \right)^2 \quad (2.55)$$

The 3 dB, or half-power, point occurs when the argument equals 1.39156, so the 3 dB beamwidth is given by

$$\lambda_{3dB} = 2\Delta\lambda_{3dB} = 0.8859 \frac{\lambda_1}{N} \quad (2.56)$$

This pattern is easily expressed in terms of frequency. Then,

$$D = \left( \frac{\sin N\pi \frac{\Delta f}{f_1}}{N\pi \frac{\Delta f}{f_1}} \right)^2 \quad (2.57)$$

and

$$f_{3dB} = 2\Delta f_{3dB} = 0.8859 \frac{f_1}{N} \quad (2.58)$$

The basic pattern, including the first five sidelobes, is plotted in Fig. 2.9 as a function of angle, Eq. (2.47), wavelength, Eq. (2.55), and frequency, Eq. (2.57). A numerical example helps to give a feel for the beamwidths involved. Thus, for  $N = 80,000$  and  $\alpha = \beta_1 = 15$  deg,  $\beta_{3dB} = 8.266 \times 10^{-5}$  rad = 0.00474 deg; if  $\alpha = \beta_1 = 30$  deg,  $\beta_{3dB} = 3.836 \times 10^{-5}$  rad = 0.00220 deg. The extreme thinness of the cone of scattered radiation is apparent; the practical concomitant is an unprecedented precision required in beam pointing.

Again, for  $N = 80,000$  and  $f_1 = 8$  GHz,  $f_{3dB} = 88.59$  kHz. This result highlights the inherent narrow-bandedness of the array. First, it gives a measure of the frequency control required because it shows, in this case, that a frequency change of only 88.59 kHz, which is roughly one part in  $10^5$  of the radiated frequency, will steer the scattered beam from one 3 dB point through the peak of the beam to the other 3 dB point. Second, it indicates that modulation should be such that the modulated signal spectrum not significantly exceed the 3 dB bandwidth of the array because the array is acting as a band-pass filter that will attenuate the distant sidebands.

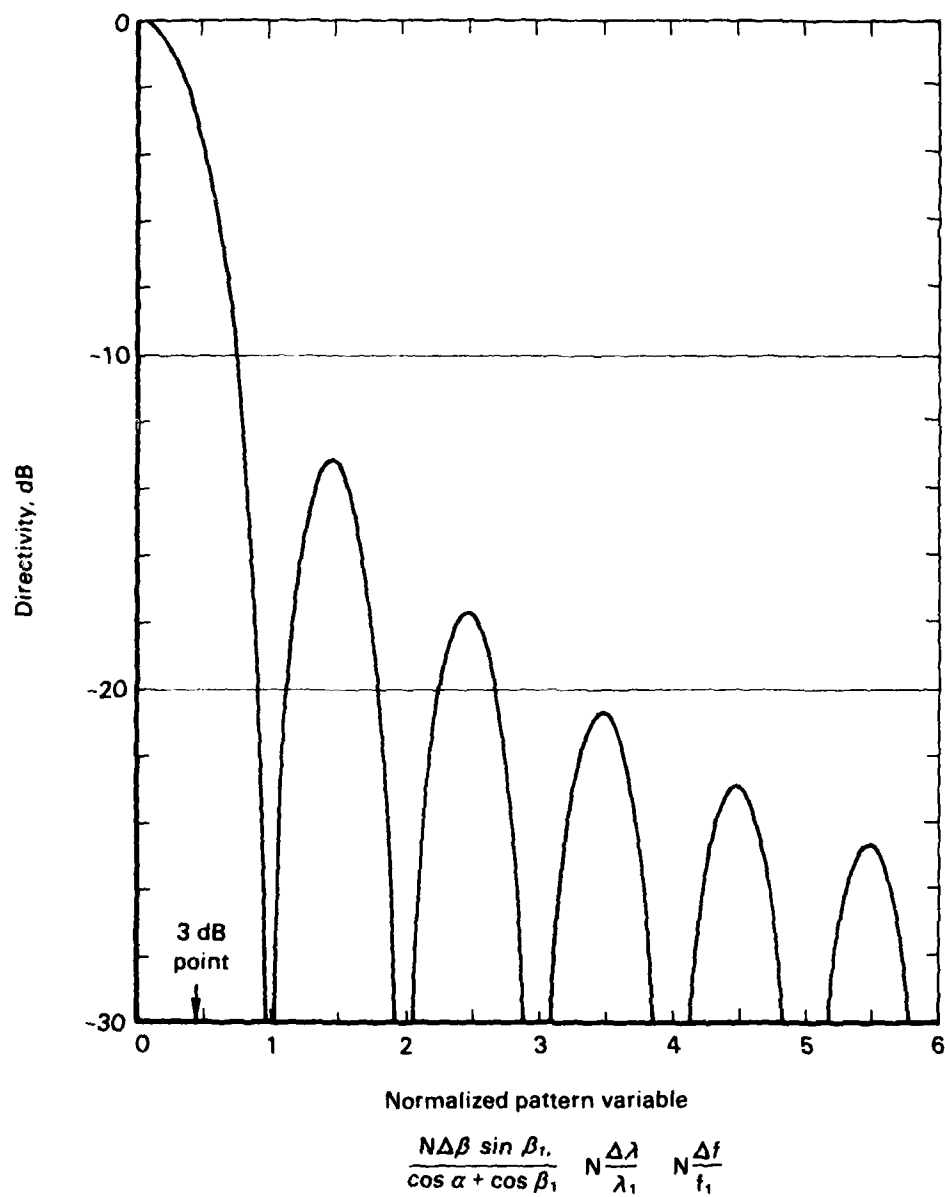


Fig. 2.9 — Far-field directivity pattern of PACSAT array

### III. QUADRATIC PHASE ERROR EFFECTS

If PACSAT were perfectly straight and at a great distance, the properties described in the preceding section would apply. However, these conditions do not obtain in practice and it is necessary to estimate the effects of nonideal operation. In this section, a quadratic phase error, which is assumed to be characteristic of small departures from ideal conditions, is introduced to display its effect on the directivity pattern and the scattering cross section. These results are then related to the specific effects associated with near-field operation and flexure of the array.

#### THE DEFOCUSING PARAMETER

In Eq. (2.19) the amplitude of the distant field was written in terms of the phase progression associated with the uniformly increasing path lengths via the various scatterers. To accommodate nearby terminals or a nonstraight array, the general form

$$|E| = \left| \sum_k \exp i \left( \frac{2\pi L_k}{\lambda} \right) \right| \quad (3.1)$$

where  $L_k$  is the path length from the transmitter to the receiver via the  $k$ th element, is needed. The path length can be expanded in a Taylor's series

$$L_k = \sum_{n=0}^{\infty} c_n k^n \quad (3.2)$$

about some convenient point, which will be taken here as the center of the array.

The initial constant  $c_0$  is readily identified as

$$c_0 = L_0 \quad (3.3)$$



where  $L_0$  is the path length from the transmitter to the receiver via the center element of the array. The first coefficient  $c_1$  gives the linear progression in path length used in Eq. (2.19). Inasmuch as interest here is centered on the behavior of the first-order grating lobe, this coefficient will be taken as

$$c_1 = \lambda_1 \quad (3.4)$$

where  $\lambda_1$  is the wavelength at which the peak of this grating lobe is formed.

Through terms of second order,

$$L_k = L_0 + \lambda_1 k + c_2 k^2 \quad (3.5)$$

Taking

$$\lambda = \lambda_1 - \Delta\lambda \quad (3.6)$$

then leads, for  $\Delta\lambda \ll \lambda_1$ , to

$$\frac{L_k}{\lambda} = \frac{L_0}{\lambda} + \left(1 + \frac{\Delta\lambda}{\lambda_1}\right) k + \frac{c_2}{\lambda_1} k^2 \quad (3.7)$$

Substituting Eq. (3.7) in (3.1) and discarding terms of unit magnitude results in

$$|E| = \left| \sum_{k=-\frac{N-1}{2}}^{\frac{N-1}{2}} \exp i 2\pi \left( \frac{\Delta\lambda}{\lambda_1} k + \frac{c_2}{\lambda_1} k^2 \right) \right| \quad (3.8)$$

where the number of elements  $N$  must be odd to place one at the center of the array.

For  $N$  large, the sum can be approximated by an integral

$$|E| = \int_{-\frac{N-1}{2}}^{\frac{N-1}{2}} \exp i 2\pi \left( \frac{\Delta\lambda}{\lambda_1} x + \frac{c_2}{\lambda_1} x^2 \right) dx \quad (3.9)$$

Completing the square and integrating leads to

$$|E| = \left| \frac{1}{2 \sqrt{\left| \frac{c_2}{\lambda_1} \right|}} \int_{U_1}^{U_2} \exp i \frac{\pi}{2} u^2 du \right| \quad (3.10)$$

where

$$U_1 = \sqrt{\left| \frac{c_2}{\lambda_1} \right|} \left[ \frac{\Delta\lambda}{c_2} - (N-1) \right], \quad U_2 = \sqrt{\left| \frac{c_2}{\lambda_1} \right|} \left[ \frac{\Delta\lambda}{c_2} + (N-1) \right] \quad (3.11)$$

When written with a lower limit of zero, the integral in Eq. (3.10) has real and imaginary parts given, respectively, by the cosine and sine Fresnel integrals

$$C(z) = \int_0^z \cos \frac{\pi}{2} t^2 dt, \quad S(z) = \int_0^z \sin \frac{\pi}{2} t^2 dt \quad (3.12)$$

Using these functions, the normalized directivity pattern becomes

$$\frac{|E|^2}{N^2} = \frac{1}{4 \left| \frac{c_2}{\lambda_1} \right| N^2} \left\{ \left[ C(U_1) - C(U_2) \right]^2 + \left[ S(U_1) - S(U_2) \right]^2 \right\} \quad (3.13)$$

At beam center  $\Delta\lambda = 0$ , and

$$\frac{|E|^2}{N^2} = \frac{1}{\left| \frac{c_2}{\lambda_1} \right| N^2} \left[ c^2(U) + s^2(U) \right] \quad (3.14)$$

where, for  $N$  large,

$$U = \sqrt{\left| \frac{c_2}{\lambda_1} \right|} N \quad (3.15)$$

Inasmuch as  $U_1$  and  $U_2$  are easily expressed in terms of  $U$  by

$$U_1 = \frac{N\Delta\lambda/\lambda_1}{U} - U, \quad U_2 = \frac{N\Delta\lambda/\lambda_1}{U} + U \quad (3.16)$$

it is seen from Eq. (3.15) that  $U$ , which will be called the defocusing parameter, completely characterizes the effect of second-order phase errors on the array performance. This is illustrated in Fig. 3.1, which shows the mainlobe and the first five sidelobes of the directivity pattern given by Eq. (3.13) for representative values of  $U$ .

The far-field, or focused pattern, which is identical to the one plotted in Fig. 2.9, results when  $U = 0$ . As the defocusing parameter is increased, the directivity (and, hence, the array scattering cross section) falls off as the sidelobe levels are raised and their structure is altered. For  $U = 1.0$ , the scattering cross section is reduced by about 1 dB, the first null is virtually eliminated, and the first sidelobe is raised by about 3 dB. The effect on higher-order sidelobes is not significant beyond about the third sidelobe.

Further increases in the defocusing parameter depress the center of the main lobe, rapidly at first, then in a steadily increasing oscillatory fashion. (This is shown in Fig. 3.2, which is a plot of Eq. (3.14).) At the same time, the first few sidelobes are radically

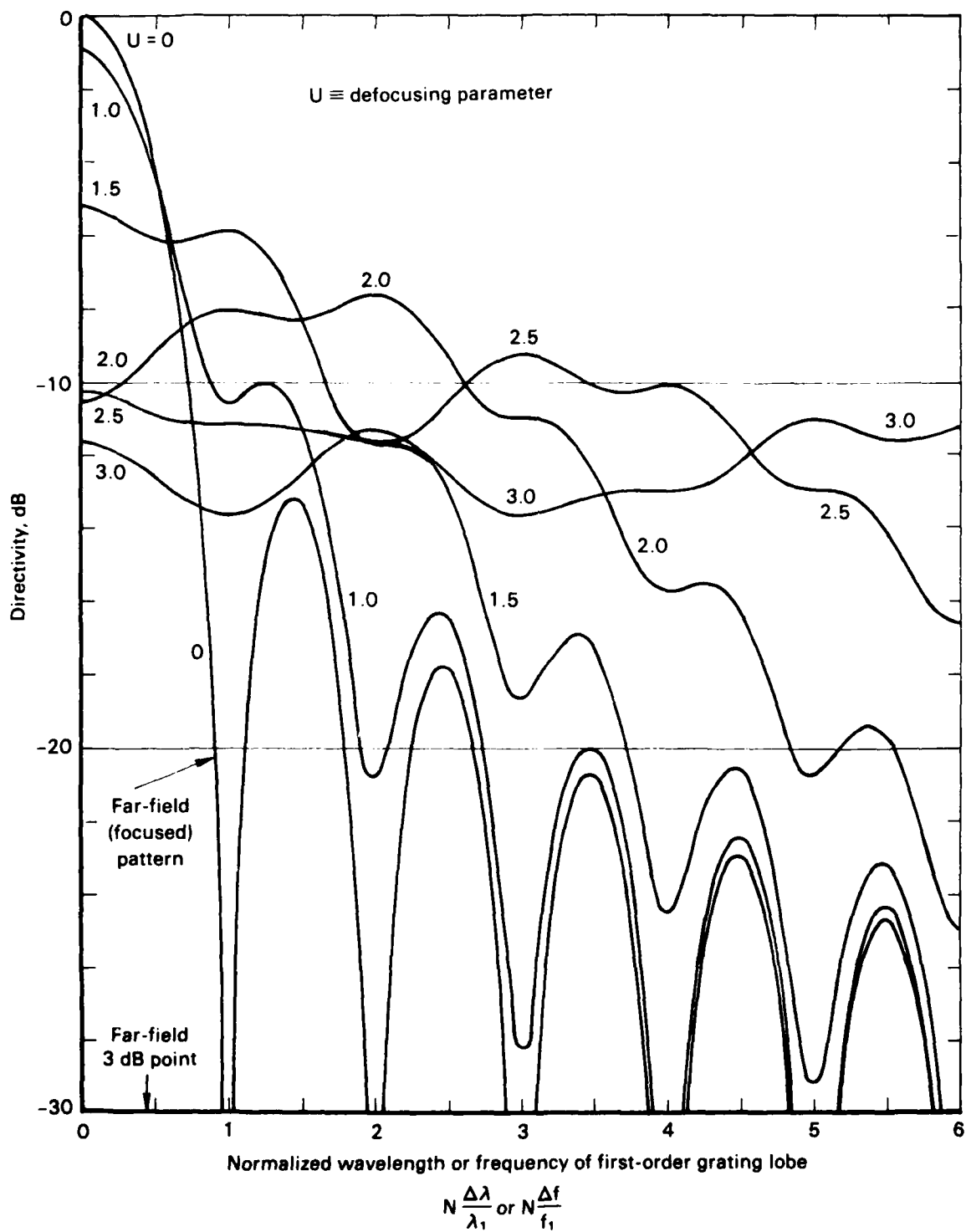


Fig. 3.1 — Directivity pattern of defocused PACSAT array

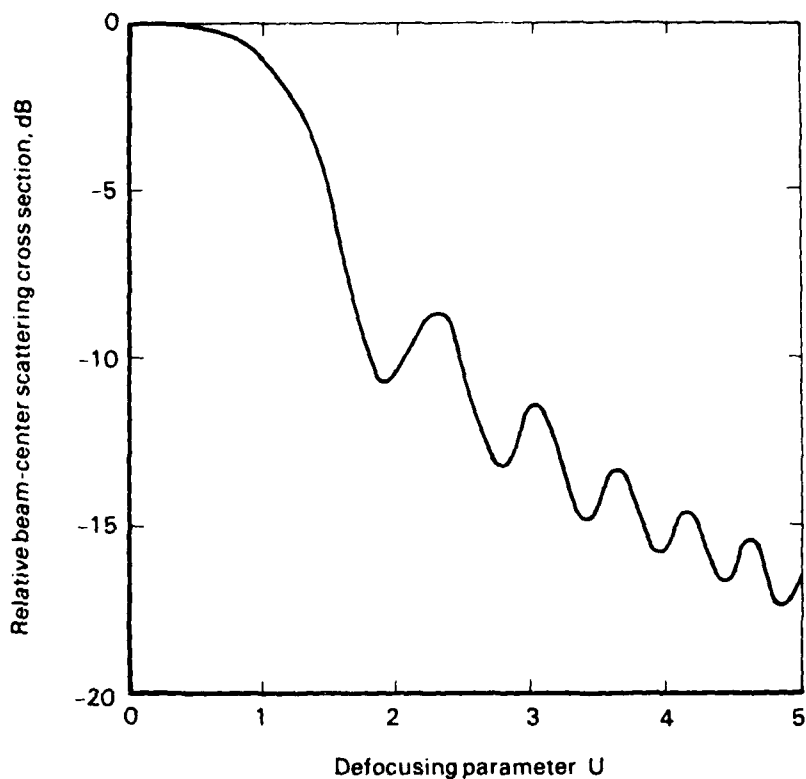


Fig. 3.2 — Scattering cross section loss for the defocused PACSAT array

affected. For example, when  $U = 2.0$ , the scattering cross section loss is about 10 dB and the first three or four sidelobes have merged into a single lobe with a 3 dB dip at its center and a 3 dB beamwidth about five times as great as that for the far-field pattern. All semblance to a normal directivity pattern in the vicinity of the main lobe is lost by the time  $U = 3.0$ . However, even large values of  $U$  have little effect on sidelobes that are well removed from the main-lobe. For instance, when  $U = 5.0$ , the 100th sidelobe has its peak value raised by only about 0.5 dB; the main effect is to fill in the nulls somewhat.\*

\*Although the 100th sidelobe may seem distant in terms of ordinary antenna practice, it should be noted, from Eq. (2.42), that the PACSAT directivity pattern has  $N$  lobes.

The general properties of the defocusing parameter, as it is related to the system parameters, are developed and discussed below. Although the choice is necessarily subjective, a value of  $U = 1.0$  will be taken here as the desirable maximum value of the defocusing parameter. It will be used in the next section to develop a tradeoff between the allowable array length, which causes near-field effects, and array flexure.

#### NEAR-FIELD OPERATION AND ARRAY FLEXURE

The factors that produce defocusing are (1) near-field operation, in which rays to or from the earth terminal to the various elements of the array can no longer be considered parallel, and, therefore, of uniformly progressive length, and (2) array flexure, which introduces additional path-length changes. Their effect is analyzed using the geometry illustrated in Fig. 3.3.

The earth, of radius  $R_e$ , is centered on the origin  $O$  of the  $x$ - $y$ - $z$  coordinate system. A terminal is assumed to be located at a point  $P$ , which is at a polar angle  $\theta$  with respect to the  $z$  axis and a meridional angle  $\phi$  with respect to the  $x$ - $z$  plane.

The PACSAT array is assumed to consist of an odd number  $N$  of elements with the center element at the origin  $O'$  of the  $x'$ - $y'$ - $z'$  coordinate system. The center element is at an altitude  $h$  above the subsatellite point  $S$ . The  $x'$  and  $y'$  axes are taken parallel to the  $x$  and  $y$  axes, respectively, and the  $z$  and  $z'$  axes are coincident. The center element is at a distance  $l_0$  from the earth point  $P$ , so the plane containing  $l_0$  and the  $z$  axis is also at a meridional angle  $\phi$  with respect to the  $x'$ - $z'$  plane. This path from  $P$  to  $O'$  forms a nadir angle  $\epsilon$  with respect to the  $z'$  axis.

The array is assumed to be flexed symmetrically into a parabolic shape and its axis is taken as the tangent at its center. The array axis is tilted at a polar angle  $\psi$  from the  $z'$  axis and is at a meridional angle  $\nu$  with respect to the  $y'$ - $z'$  plane. The plane containing the flexed array is at an angle  $\omega$  with respect to the plane containing the array and  $z'$  axes.

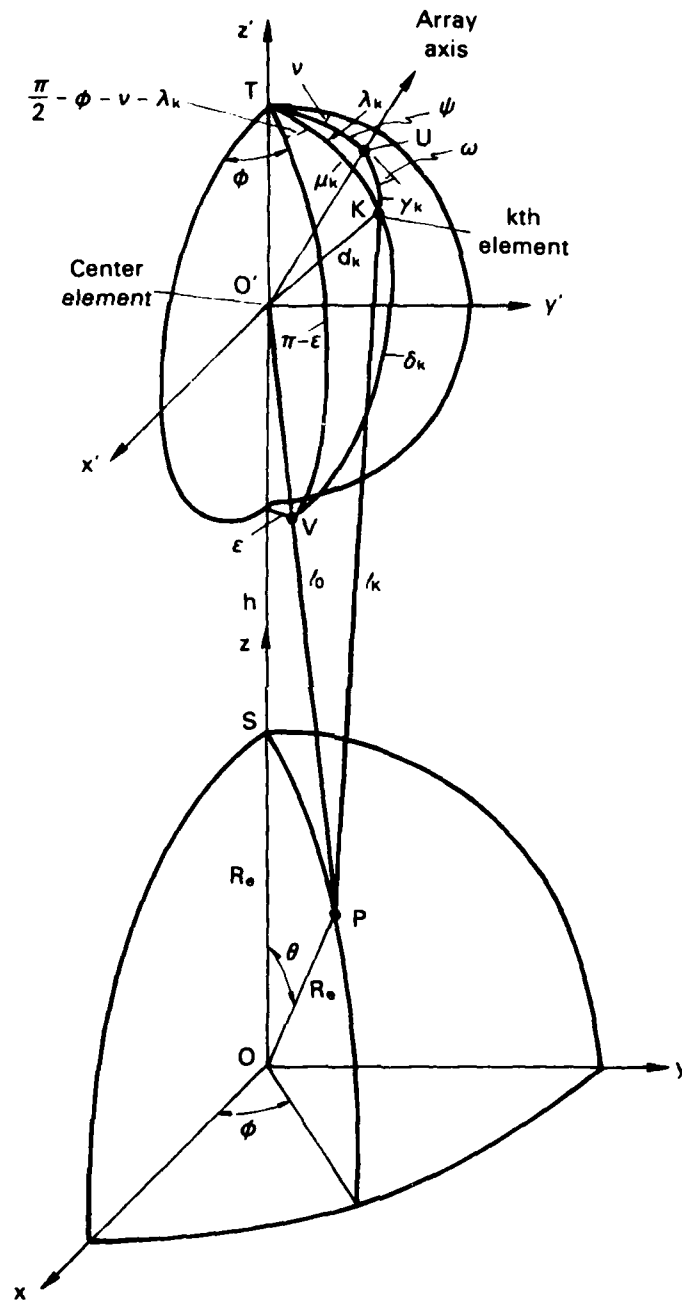


Fig. 3.3 — Geometry of PACSAT in orbit when tilted and flexed

The  $k$ th element of the array is at the point  $K$  a distance  $d_k$  from the center element and a distance  $\ell_k$  from the point  $P$ . The lines from  $O'$  to  $K$  and the array axis form an angle  $\gamma_k$ . A sphere of radius  $d_k$  is centered on the  $x'-y'-z'$  coordinate system; its intersections with the  $+z'$  axis, the array axis, and the line from  $P$  to  $O'$  are designated by  $T$ ,  $U$ , and  $V$ , respectively.

The polar angle  $\mu_k$  to the line from  $O'$  to  $K$  together with  $\psi$  and  $\gamma_k$ , which have already been defined, form the sides of the oblique spherical triangle,  $TUK$ ; the included angle at  $T$  is denoted by  $\lambda_k$ . The great circle from  $K$  to  $V$  completes another oblique spherical triangle,  $TKV$ , whose sides are  $\mu_k$ ,  $\delta_k$ , and  $\pi - \epsilon$  and whose included angle at  $T$  is equal to  $\pi/2 - \phi - \nu - \lambda_k$ .

The geometry shown in Fig. 3.3 is general and bears no relationship to a particular orbit for PACSAT. In the next section, when results will be specialized for a circular equatorial orbit, the  $y$ -axis will become the earth's polar axis and the  $x$ - $z$  plane will become the equatorial plane. The unusual orientation used in Fig. 3.3 was chosen to afford the clearest perspective of the various angles and distances that are involved.

In the following analysis, the path length  $L_k$  from a point  $P_1$  to another point  $P_2$  via the  $k$ th scatterer will be calculated as a power series in  $k$ , as was indicated in Eq. (3.2). The coefficient  $c_2$  of the term in  $k^2$  will then serve to express the defocusing parameter  $U$  from Eq. (3.15) in terms of the significant geometrical factors shown in Fig. 3.3. As suggested above, the subscripts 1 and 2 will be used to identify those factors that are associated with the points  $P_1$  and  $P_2$ , respectively. The expansion will include near-field effects by assuming that  $d_k$  is sufficiently small in comparison with  $\ell_0$  that only the leading terms in  $d_k/\ell_0$  need be retained. Similarly, flexure effects will be included by assuming that  $\gamma_k$  is sufficiently small that only leading terms in  $\gamma_k$  need be retained.

#### Basic Expressions

There are no limitations on the meridional angle  $\phi$  of the point  $P$ . Its polar angle  $\theta$ , however, is limited to the value at which  $P$  is on the horizon. This occurs when



$$\cos \theta_{\max} = \frac{R_e}{R_e + h} \quad (3.17)$$

From the triangle  $OO'P$ , the path length  $\ell_0$  to the center element of the array is given by

$$\ell_0^2 = R_e^2 + (R_e + h)^2 - 2R_e(R_e + h) \cos \theta \quad (3.18)$$

and the nadir angle  $\epsilon$  by

$$\sin \epsilon = \left( \frac{R_e}{\ell_0} \sin \theta \right) \quad (3.19)$$

The path length  $\ell_k$  from  $P$  to the  $k$ th element of the array is found from the triangle  $O'KP$  as

$$\ell_k^2 = \ell_0^2 + d_k^2 - 2\ell_0 d_k \cos \delta_k \quad (3.20)$$

Expanding in powers of  $d_k$  leads to

$$\ell_k = \ell_0 - d_k \cos \delta_k + \frac{1}{2} \frac{d_k^2}{\ell_0} \sin^2 \delta_k + O\left(\frac{d_k^3}{\ell_0^3}\right) \quad (3.21)$$

The term  $\cos \delta_k$  is found from the spherical triangle  $VTK$  as

$$\cos \delta_k = -\cos \epsilon \cos \mu_k + \sin \epsilon \sin \mu_k \times$$

$$\left[ \sin(\phi + \nu) \cos \lambda_k + \cos(\phi + \nu) \sin \lambda_k \right] \quad (3.22)$$

From the spherical triangle  $TUK$  it is seen that

$$\cos \mu_k = \cos \psi \cos \gamma_k - \sin \psi \sin \gamma_k \cos \omega$$

$$\sin \mu_k = \frac{\sin \gamma_k \sin \omega}{\sin \lambda_k} \quad (3.23)$$

$$\cos \gamma_k = \cos \psi \cos \mu_k + \sin \psi \sin \mu_k \text{ and } \lambda_k$$

Substituting Eqs. (3.23) in Eq. (3.22) leads, after some manipulation, to

$$\cos \delta_k = h \cos \gamma_k + \sin \gamma_k \quad (3.24)$$

where

$$h = -\cos \epsilon \cos \psi + \sin \epsilon \sin (\phi + \nu) \sin \psi$$

$$j = \cos \epsilon \sin \psi \cos \omega + \sin \epsilon \sin (\phi + \nu) \cos \psi \cos \omega \quad (3.25)$$

$$+ \sin \epsilon \cos (\phi + \nu) \sin \omega$$

Expanding Eq. (3.24) in powers of  $\gamma_k$  then leads to

$$\cos \delta_k = h + j \gamma_k - \frac{1}{2} h \gamma_k^2 + O(\gamma_k^3) \quad (3.26)$$

$$\sin^2 \delta_k = (1 - h^2) - 2hj \gamma_k + (h^2 - j^2) \gamma_k^2 + O(\gamma_k^3)$$

which are needed in Eq. (3.21).

### Parameters of the Flexed Array

The array of length  $L$  is assumed to be flexed in the shape of a plane parabola of maximum deflection  $D$  as shown in Fig. 3.4. The  $x$  axis corresponds to the array axis in Fig. 3.3. As before, the number of elements  $N$  is taken as odd so that there is an element at the center. The array length is related to the number of elements and their spacing  $s$  by

$$L = (N - 1)s \quad (2.39)$$

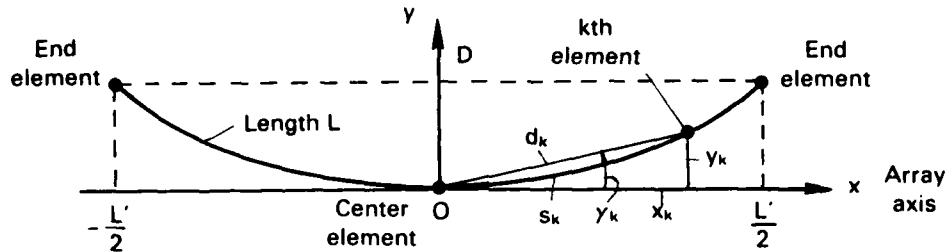


Fig. 3.4 — Geometry of the flexed array

To facilitate the analysis, it will be assumed that the array flexes smoothly. The rectilinear distance  $s_k$  along the array from its center to the  $k$ th element, which is given by

$$s_k = sk, \quad k = -\frac{N-1}{2}, \dots, 0, \dots, \frac{N-1}{2} \quad (3.27)$$

can then be written as the curvilinear distance

$$s(t) = t, \quad -\frac{L}{2} < t < \frac{L}{2} \quad (3.28)$$

where  $t$  is a running variable along the array.

Let  $L'$  denote the length of the array projected on the x axis. It can be shown for  $D \ll L$  that a negligible error will result by using  $L$  for  $L'$ . The array is then described by

$$y(t) = \frac{4D}{L^2} x^2(t) \quad (3.29)$$

To obtain a parametric representation of a point on the array, note that the differential length  $ds$  along the array can be written

$$\left(\frac{ds}{dt}\right)^2 = \left(\frac{dx}{dt}\right)^2 + \left(\frac{dy}{dt}\right)^2 \quad (3.30)$$

Using Eq. (3.28) for  $s$  and Eq. (3.29) for  $y$  yields

$$\frac{dx}{dt} = 1 - \frac{1}{2} \left(\frac{8Dx}{L^2}\right)^2 + O\left(\frac{8Dx}{L^2}\right)^4 \quad (3.31)$$

It can be shown that the solution to Eq. (3.31) is given by

$$x(t) = t \left[ 1 - \frac{32}{3} \left(\frac{Dt}{L^2}\right)^2 + O\left(\frac{Dt}{L^2}\right)^4 \right] \quad (3.32)$$

Using Eq. (2.39) to eliminate  $L$  and Eqs. (3.27) and (3.28) to reintroduce  $k$  leads to

$$\mathcal{D} \equiv \frac{Dt}{L^2} = \frac{Dk}{s(N-1)} \ll 1 \quad (3.33)$$

Thus, Eq. (3.32) can be written

$$x_k = sk \left[ 1 - \frac{32}{3} \rho^2 + O(\rho^4) \right] \quad (3.34)$$

and, from Eq. (3.29),

$$y_k = 4 sk \rho \left[ 1 - \frac{64}{3} \rho^2 + O(\rho^4) \right] \quad (3.35)$$

The distance  $d_k$  and the angle  $\gamma_k$  to the  $k$ th element are then found to be

$$d_k = \sqrt{x_k^2 + y_k^2} = sk \left[ 1 - \frac{8}{3} \rho^2 + O(\rho^4) \right] \quad (3.36)$$

and

$$\gamma_k = \tan^{-1} \frac{y_k}{x_k} = 4\rho \left[ 1 - 16 \rho^2 + O(\rho^4) \right] \quad (3.37)$$

which, noting Eq. (3.33), are the desired expansions in powers of  $k$ .

#### The Path-Length Expansion

The terms  $\cos \delta_k$  and  $\sin^2 \delta_k$  in Eqs. (3.26) are found by substituting from Eq. (3.37)

$$\cos \delta_k = h + 4j\rho - 8h\rho^2 + O(\rho^3)$$

$$\sin^2 \delta_k = (1 - h^2) - 8hj\rho + O(\rho^2) \quad (3.38)$$

These, together with Eq. (3.36) for  $d_k$ , then give the path length  $l_k$  in Eq. (3.21) as

$$\begin{aligned} \ell_k = \ell_0 - shk + \left[ \frac{s^2}{2} \frac{1-h^2}{\ell_0} - \frac{4D}{(N-1)^2} \right] k^2 \\ - \frac{4sD}{(N-1)^2} \frac{hj}{\ell_0} k^3 + O(k^4) \end{aligned} \quad (3.39)$$

where Eq. (3.33) has been used to eliminate  $\mathcal{B}$ .

For practical values of  $D$ ,  $s$ ,  $N$ , and  $\ell_0$ , the term in  $k^3$  is negligible so the total path length  $L_k$  from the point  $P_1$  to the point  $P_2$  via the  $k$ th element is given by

$$\begin{aligned} L_k = (\ell_{0_1} + \ell_{0_2}) - s(h_1 + h_2)k \\ + \left[ \frac{s^2}{2} \left( \frac{1-h_1^2}{\ell_{0_1}} + \frac{1-h_2^2}{\ell_{0_2}} \right) - \frac{4D}{(N-1)^2} (j_1 + j_2) \right] k^2 \end{aligned} \quad (3.40)$$

where the subscripts identify terms as they are related to the two points, and where  $h$  and  $j$  are given by Eqs. (3.25).

A comparison of Eq. (3.40) with Eqs. (3.2) to (3.5) shows that

$$\begin{aligned} c_0 = L_0 = \ell_{0_1} + \ell_{0_2} \\ c_1 = \lambda_1 = -s(h_1 + h_2) \end{aligned} \quad (3.41)$$

$$c_2 = \left[ \frac{s^2}{2} \left( \frac{1-h_1^2}{\ell_{0_1}} + \frac{1-h_2^2}{\ell_{0_2}} \right) - \frac{4D}{(N-1)^2} (j_1 + j_2) \right]$$

The first of these is as expected. The second establishes the relationships between the basic PACSAT incidence and first-order grating lobe angles  $\alpha$  and  $\beta_1$ , respectively. From Eq. (2.24) it is seen that

$$\cos \alpha = -h_1, \quad \cos \beta_1 = -h_2 \quad (3.42)$$

### The Defocusing Parameter

The third of Eqs. (3.41) provides the coefficient  $c_2$  needed to calculate the defocusing parameter  $U$  from Eq. (3.15). Although this formulation, which is expressed in terms of the basic geometric system parameters, is suitable for numerical evaluation, it does not lend itself to an interpretation of how the near-field and flexure parameters contribute to defocusing. To obtain such a form, it is necessary to simplify the parameters  $j_1$  and  $j_2$  in a fashion similar to that done with  $h_1$  and  $h_2$  in Eqs. (3.42).

The simplified geometry of the tilted and flexed array is shown in Fig. 3.5, which is similar to the upper portion of Fig. 3.3. The

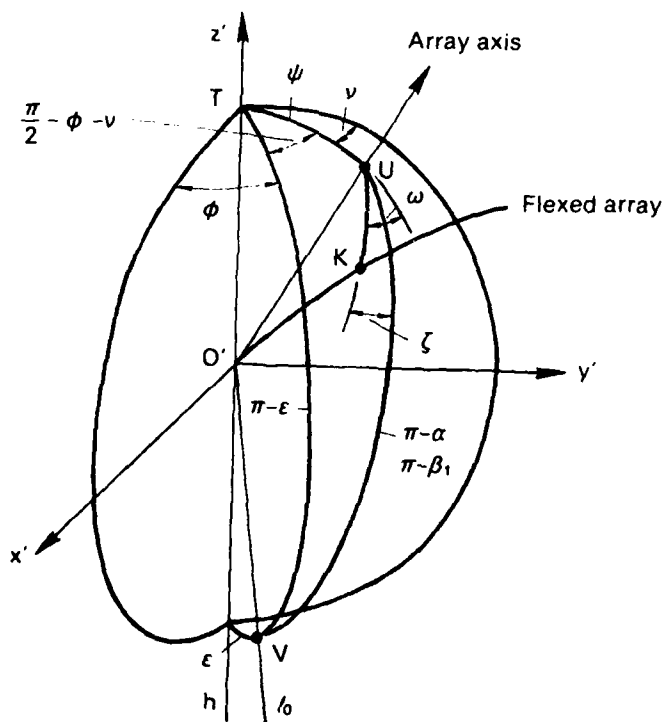


**Fig. 3.5 — Simplified geometry of the tilted and flexed array**

flexed array is shown as an arc from the origin  $O'$  passing through a point  $K$ . The array axis and the flexed array then define the plane in which the array is tilted. Note that the angle  $VO'U$  is equal to  $\pi - \alpha$  or  $\pi - \beta_1$  depending on whether the point on the earth, which is not shown, is the transmitter or the receiver, respectively. Thus, the array axis and the line of length  $\ell_0$  from  $O'$  to the earth point define the plane of illumination (or scattering).

Let the  $\zeta$  denote the angle between the plane of illumination (or scattering) and the plane of flexure. It can be shown that

$$j_1 = \sin \alpha \cos \zeta_1, \quad j_2 = \sin \beta_1 \cos \zeta_2 \quad (3.43)$$

Then, using Eq. (2.39) to reintroduce the array length  $L$  and Eqs. (3.42) and (3.43) to eliminate  $h$  and  $j$  brings the defocusing parameter in Eq. (3.15) into the form

$$U^2 = \left| \frac{L^2}{\lambda_1} \left( \frac{\sin^2 \alpha}{2\ell_{01}} + \frac{\sin^2 \beta_1}{2\ell_{02}} \right) - \frac{4D}{\lambda_1} (\sin \alpha \cos \zeta_1 + \sin \beta_1 \cos \zeta_2) \right| \quad (3.44)$$

where the third of Eqs. (3.41) was used for  $c_2$ .

The first group of terms in Eq. (3.44) exhibits the effects of near-field operation. As the array length  $L$  is increased in relation to the wavelength  $\lambda_1$  and the array center path lengths  $\ell_{01}$  and  $\ell_{02}$ , these terms increase the value of the defocusing parameter. It is interesting to note that  $L \sin \alpha$  and  $L \sin \beta_1$  are the projected lengths of the array in the directions of illumination and scattering, respectively. Thus, near-field effects are reduced as end-fire operation is approached. One of the adverse effects of libration is that the near-field effect is exacerbated when the array is at the less favorable orientations. It should be noted that  $\alpha$  and  $\beta_1$  vary during the transit of an array in orbit, even if there is no libration.



For equal path lengths, the term  $[(L \sin \alpha)^2 + (L \sin \beta_1)^2]/2\lambda_1$  is equal to the average of the ratios of the squares of the projected array length to the operating wavelength. Thus, the near-field term in Eq. (3.44), when equated to unity, is analogous to the approximation  $R = D^2/\lambda$  used in aperture theory to denote the range  $R$  at which the transition from the Fresnel (near-field) to the Fraunhofer (far-field) regions occurs. That is to say, the value  $U = 1.0$  mentioned above as the desirable maximum allowable value for  $U$  is consistent, in the absence of flexure, to operation of the PACSAT array in the transition region.

The second group of terms in Eq. (3.44) displays the effects of array flexure. Unlike the near-field terms, which are nonnegative, the flexure terms can be negative and can, therefore, actually compensate for near-field effects to some extent. Thus, they can focus the array as well as defocus it. To appreciate this, note from Fig. 3.5 that if  $\zeta$  is near zero, the array is flexed so as to present a concave, or focusing, aspect along the line of sight. Conversely, if  $\zeta$  is near  $\pi$ , the aspect is convex, or defocusing. As with the near-field terms, the factors  $\sin \alpha$  and  $\sin \beta_1$  indicate that flexure effects are reduced as end-fire operation is approached.

#### The Flexure-Length Tradeoff

The form of the defocusing parameter in Eq. (3.44) suggests that a tradeoff exists between the defocusing produced by flexure and that produced by near-field operation. To illustrate this tradeoff, consider a pair of users at 38 deg latitude separated by 38 deg in longitude. (These locations are 3310 km apart at a mid-U.S. latitude. They are roughly midway among the various user pairs in the next section (see Fig. 4.5) that illustrate various system parameters for PACSAT in a circular equatorial orbit.)

Let PACSAT be at an altitude  $h$  above the equator at a longitude midway between the users. Further, let the array be tilted, i.e., librated, toward the north at angle  $\psi$  so that it presents a maximum projected length toward the users ( $\nu = 0$  in Fig. 3.5). Finally, let the array be flexed toward the south so as to present a convex or

defocusing aspect toward the users ( $\omega = \pi$  in Fig. 3.5). Although this is probably not a worst-case configuration (the users should be nearer one another and at some pessimum latitude), it is nonetheless one that is highly unfavorable and, therefore, suitable for illustrating the adverse effects of defocusing.

The tradeoff is plotted in Fig. 3.6, which shows how the normalized array length  $L^2/\lambda_1 R_e$  can be traded off against the normalized flexure  $D/\lambda_1$  for a constant value of 1.0 for the defocusing parameter.

The most striking thing to be noted from Fig. 3.6 is that the flexure cannot be allowed to exceed a fraction of a wavelength for the range of parameters considered, even if there were no near-field effects. If practical array lengths are assumed, the near-field effect further reduces the flexure that can be tolerated. The straightness criterion is therefore seen to be stringent; for example, an eighth of a wavelength is less than 5 mm at 8 GHz. Orbiting an array that departs from linearity by no more than such an amount over a length of 1000 m or more will be a formidable task.

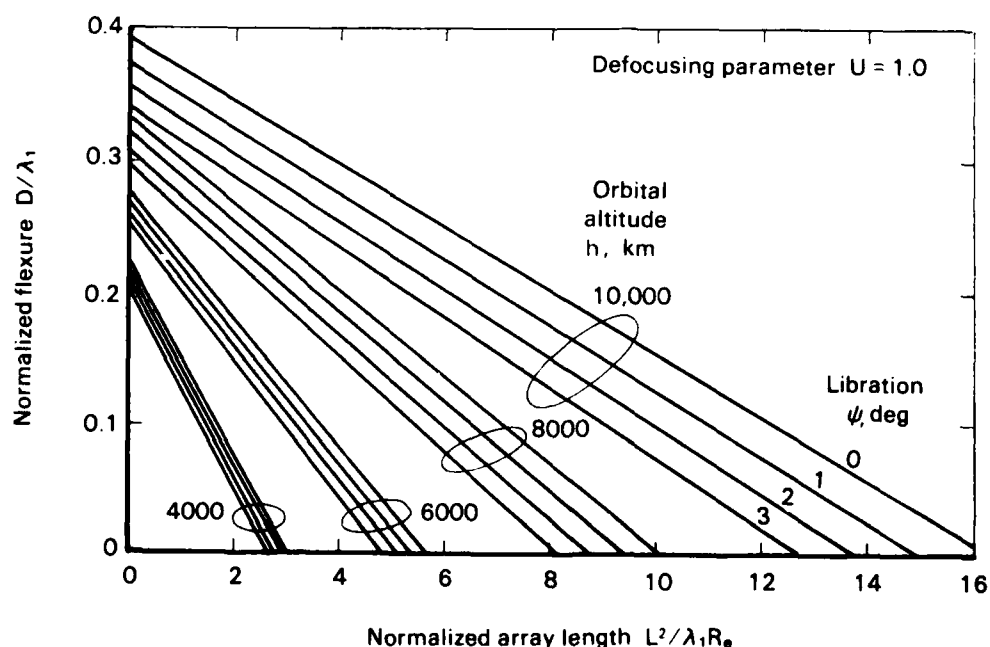


Fig. 3.6 — Near-worst-case, flexure/length tradeoff: users at 38 deg latitude separated 38 deg in longitude and array at midlongitude over equator

The significance of the limitation in the normalized array length  $L^2/\lambda_1 R_e$  can be appreciated from Fig. 3.7, which shows how it is

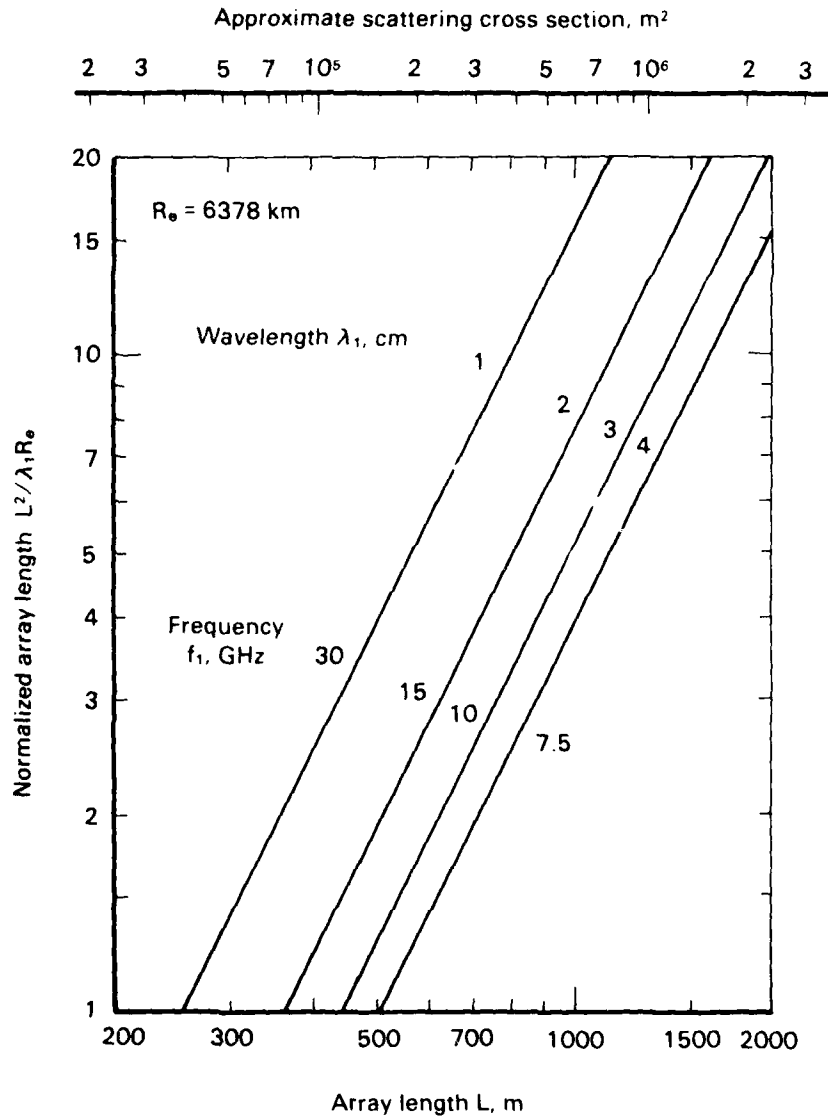


Fig. 3.7 — Normalized array length

related to the actual array length at a given operating frequency. Consider, for instance, a system operating at an orbital altitude of 8000 km. If it were felt that the array flexure could be limited to an eighth of a wavelength and the array libration to two degrees, the tradeoff in Fig. 3.6 shows that the normalized array length must not exceed a value of about 5.2. From Fig. 3.7 it is seen that the array length would be limited to about 1100 m if the operating frequency were 8 GHz. The scale at the top of Fig. 3.7, which is constructed according to the approximation  $\sigma \approx 0.6L^2$  (see Eq. (4.15)) shows that an array of that length would have a scattering cross section of about 725,000 m<sup>2</sup>.

The specific values cited above must, of course, be taken in context because they relate to a specific user and orbital geometry that may or may not be worst case; to an array configuration and behavior (i.e.,  $\lambda/8$  flexure and 2 deg libration) that may or may not be achieved; and to a defocusing criterion (i.e.,  $U = 1.0$ ) that is subjective to some extent. The important conclusions are that (1) the array must be straight to within a fraction of a wavelength; (2) the libration should be limited to a few degrees, at most;\* and (3) the normalized array length  $L^2/\lambda_1 R_e$  must not exceed a value on the order of 10. If these conditions are not satisfied, significant reductions in scattering cross section and distortions of the scattered beam (in the vicinity of the mainlobe) will occur under some unfavorable circumstances.

---

\*It will be shown in the next section that excessive libration also exacerbates the system bandwidth requirement problem.

#### IV. PACSAT IN A CIRCULAR EQUATORIAL ORBIT

The desirability of a circular equatorial orbit for PACSAT was mentioned in the Synopsis. In fact, circularity is mandatory because gravity-gradient stabilization, which is used to keep the array erect, will not work in an elliptical orbit. Placing the circular orbit in the equatorial plane offers important system advantages that outweigh the loss of polar coverage provided only by satellites in inclined orbits; at the orbital altitudes suitable for use by PACSAT, coverage can be provided up to the midlatitudes. Thus, strategic command and control communications that require CONUS coverage can be satisfied.

A practical system must incorporate enough satellites to provide continuous service. To form a communication link, a pair of users must acquire a predetermined satellite as it comes into mutual view, then track it during its transit. At some point the satellite must be relinquished and another acquired to maintain continuity. Inasmuch as satellites in circular equatorial orbits make identical transits as viewed by a given user, the antenna pointing problem for acquisition and tracking is simplified. Furthermore, only a limited segment of the celestial sphere need be viewed, thereby facilitating terminal siting and antenna design in some instances.

Another advantage of the circular equatorial orbit is that the PACSAT design uses a frequency steerable beam to form a communication link. As noted in connection with Eq. (1.1), the appropriate operating wavelength depends on the illumination and scattering angles  $\alpha$  and  $\beta_1$ . If these angles are allowed to assume the wide range of values that can result when inclined orbits are used, the operating bandwidth can greatly exceed available allocations. It is a characteristic of the circular equatorial orbit that, for users at midlatitudes, the values of  $\alpha$  and  $\beta_1$  vary in such a way during the course of a satellite transit that the sum of their cosines is nearly constant. (In fact, the bandwidth requirement will depend principally on the amount of libration the array experiences.) Thus, the use of circular equatorial orbits reduces the required operating bandwidth to a

practical amount and eases the frequency, as well as the spatial, acquisition and tracking problem.

In this section, the orbital properties of satellites in circular equatorial orbits are reviewed and the important geometrical relationships to viewers at typical locations are developed. This is followed by an examination of the pertinent electromagnetic or communication characteristics. These are then used to illustrate a typical array design. Finally, the link equation is derived and typical power budgets are presented.

### GEOMETRICAL AND ORBITAL PROPERTIES

#### Orbital Rate and Period

The links for PACSAT in a circular equatorial orbit are illustrated in Fig. 4.1. The earth is centered on the origin of the x-y-z coordinate system with the polar axis coinciding with the z axis. The earth is rotating at an angular rate  $\Omega$  equal to  $7.2921 \times 10^{-5}$  rad/sec, which is the rate corresponding to the 23 hr 56 min 4.1 sec sidereal day. However, the coordinate system is assumed to be fixed to the earth with the Greenwich meridian in the x-z plane. PACSAT is shown in the x-y, or equatorial, plane at a constant altitude  $h$  above the surface of the earth and is assumed to be in a progressive orbit, i.e., rotating in the same direction as the earth.

The orbital angular rate for an earth satellite relative to inertial space is given by

$$\omega = \sqrt{\frac{\mu}{r^3}} \text{ rad/sec} \quad (4.1)$$

where  $r$  is the orbital radius and  $\mu = 1.4076 \times 10^{16} \text{ ft}^3/\text{sec}^2$ . Converting to kilometers and introducing the altitude  $h$  and the radius of the earth  $R_e$  yields

$$\omega = \frac{6.3135 \times 10^2}{(h + R_e)^{3/2}} \text{ rad/sec} \quad (4.2)$$

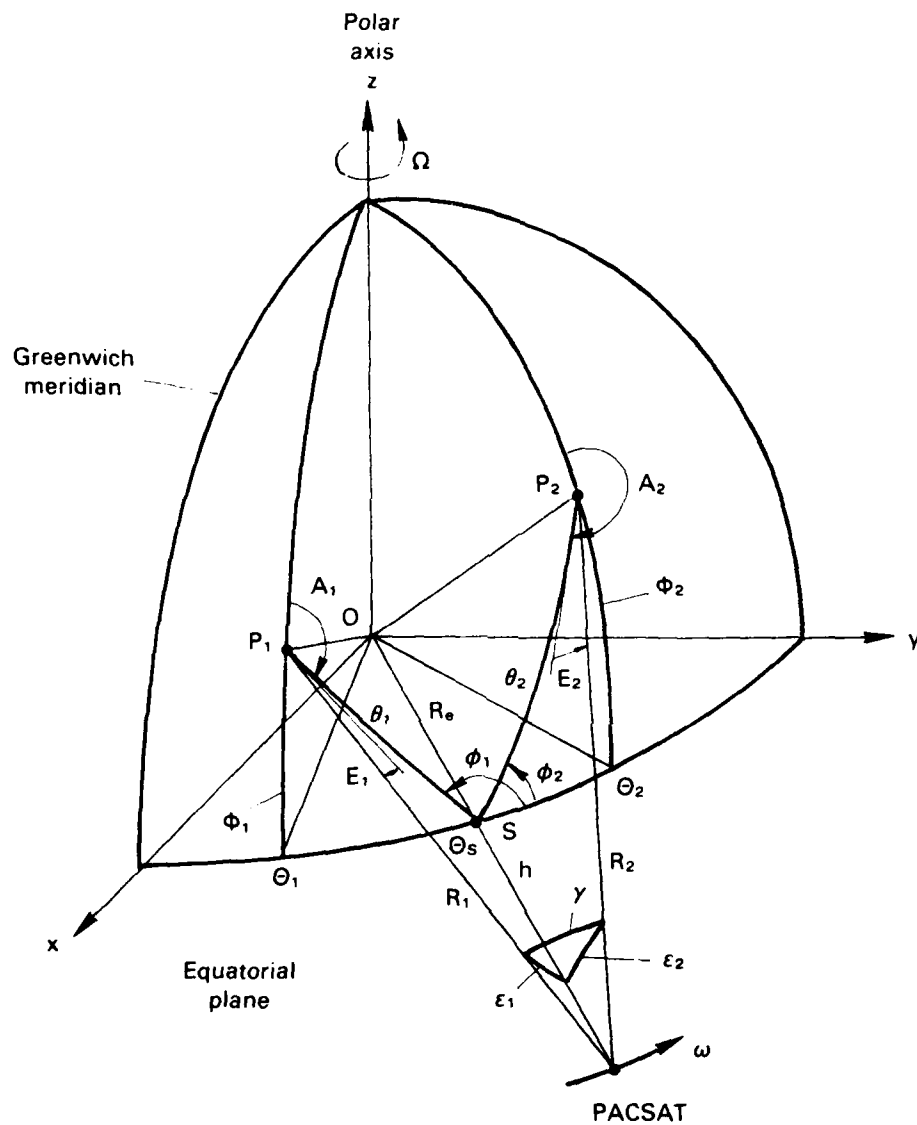


Fig. 4.1 — Link geometry for PACSAT in a circular equatorial orbit

where  $R_e \approx 6378$  km. This orbital period  $2\pi/\omega$  in hours is plotted on Fig. 4.2 for a range of orbital altitudes from 3000 to 10,000 km, which encompasses those of interest for PACSAT. Let  $\theta_s$  denote the longitude of the satellite. Then, the orbital rate relative to the

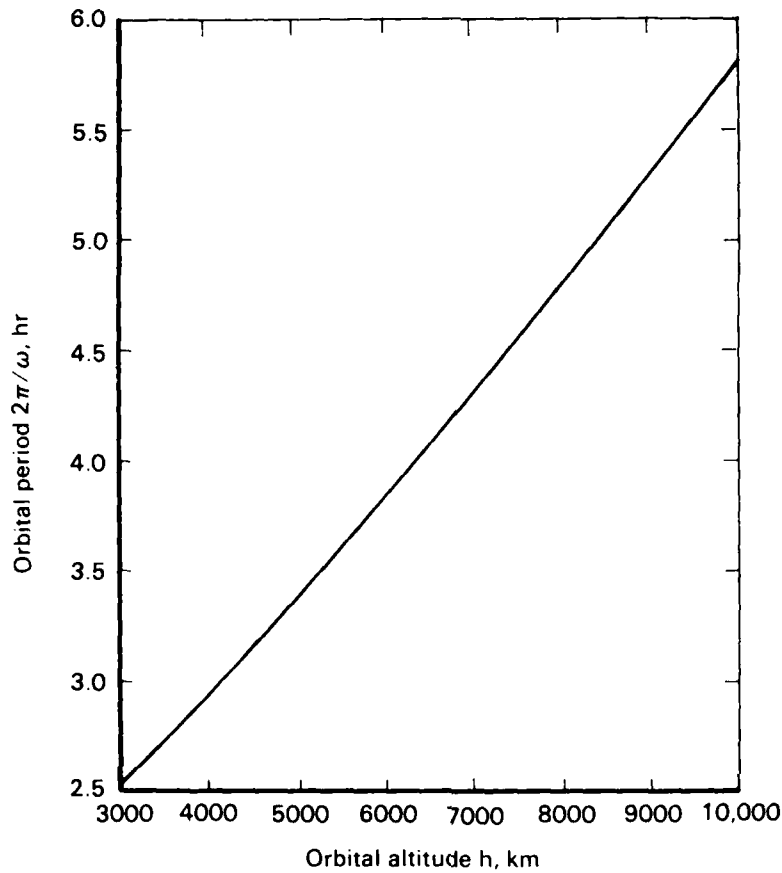


Fig. 4.2 — Orbital period for a satellite in a circular orbit

earth is given by

$$\dot{\theta}_S = \omega - \Omega \quad (4.3)$$

This is plotted on Fig. 4.3 in deg/min.

#### Coverage

Typical users are shown in Fig. 4.1 at points  $P_1$  and  $P_2$ , which are at latitudes and longitudes  $\phi_1, \theta_1$  and  $\phi_2, \theta_2$ , respectively. The lines of sight from these users to the array form a bistatic scattering angle  $\gamma$  and the bearing angles  $\epsilon_1$  and  $\epsilon_2$ . If the array is erect,



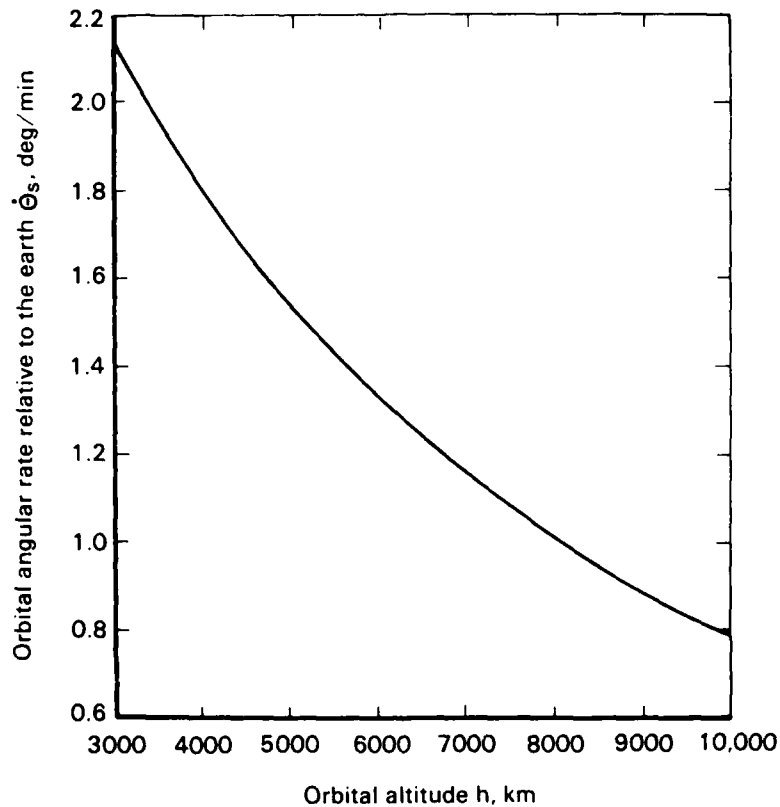


Fig. 4.3 — Orbital angular rate relative to the earth for a satellite in a circular equatorial orbit

these become the incidence and scattering angles  $\alpha$  and  $\beta_1$  as shown in Fig. 1.1. The great circles from these points to the subsatellite point form polar and meridional angles  $\theta_1, \phi_1$  and  $\theta_2, \phi_2$ , respectively, as also shown in Fig. 3.3. These angles are related to the various latitudes and longitudes by

$$\cos \theta = \cos (\theta_P - \theta_S) \cos \phi_P$$

(4.4)

$$\tan \phi = \frac{\tan \phi_P}{\sin (\theta_P - \theta_S)}$$

where the appropriate numerical subscripts are to be added as required.

The satellite appears at the horizon to a given user when its line of sight is tangent to the surface of the earth. At that point

$$\cos \theta_{\max} = \frac{R_e}{R_e + h} \quad (3.17)$$

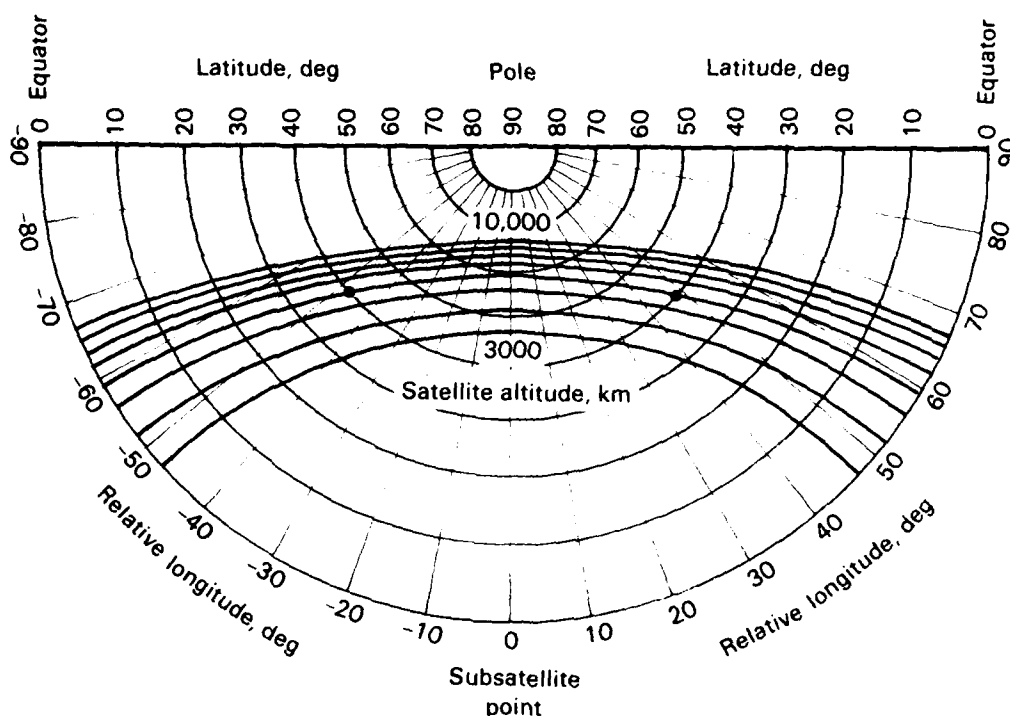
so, using Eq. (4.4), the satellite longitudes at the extremes of its visibility are given by

$$\theta_S = \theta_P \pm \cos^{-1} \left[ \frac{R_e}{(R_e + h) \cos \phi_P} \right] \quad (4.5)$$

For the progressive satellite motion depicted in Fig. 4.1, the longitude at which the satellite rises is obtained by using the minus sign in Eq. (4.5); the longitude of setting then comes from using the plus sign.

The coverage afforded by a satellite in an equatorial orbit is shown in Fig. 4.4, which is a portion of a polar stereographic projection [6]. The plane of the projection is tangent to the earth at one pole, and the point from which the projection is developed is the other pole. Such a projection is conformal and, hence, has the property that circles on the earth are projected into circles. Thus, coverage areas, which, of course, are circles, are projected as circles rather than the distorted figures usually seen on other projections.

The projection in Fig. 4.4 is limited to one hemisphere, so the outer circular arc of the plot is the equator. The coverage circles show the portion of the earth visible at various altitudes from a satellite at the indicated subsatellite longitude. With respect to the coverage circle associated with a particular orbital altitude, a user will be in view of the satellite if he is within the coverage circle. If the user is on the coverage circle, the satellite will appear to be on the horizon. The two longitudes at which a user at a given latitude can be on the coverage circle are separated by the



• Points used in the text example.

Fig. 4.4 — Coverage contours for a satellite in an equatorial orbit

difference in rising and setting satellite longitudes given by Eq. (4.5). For example, consider a user at a latitude of 40 deg and a satellite at an altitude of 6000 km; the two relative satellite longitudes at which that user would observe the satellite at the horizon are shown by dots on Fig. 4.4. The separation in longitude is seen to be 95.5 deg, which is equal to twice the inverse cosine term in Eq. (4.5).

Because of the potential application of PACSAT within the continental United States, it is convenient to define a generalized service area that approximates the United States in shape. User locations at the extremities of this area can then be paired to illustrate the significant system parameters to be developed below. The service

area will be assumed to extend 45 deg in longitude between 30 and 45 deg N latitude. This area is shown superposed over the United States on the polar stereographic projection in Fig. 4.5. The circles at the corners of this area are user locations that form the following pairs:

1. Both users at 30 deg latitude separated by 45 deg in longitude.
2. One user at 30 deg latitude and the other at 45 deg latitude separated by 45 deg in longitude.
3. Both users at 45 deg latitude separated by 45 deg in longitude.

These will be used to illustrate some of the system parameters developed in the following. The results that do not require specification of a user pair will be presented for users at 30 deg and 45 deg latitude. The user pair located at 38 deg latitude separated by 38 deg in longitude chosen to illustrate the flexure/length tradeoff in Fig. 3.6 is indicated by stars in Fig. 4.5.

#### Transit Trajectories

The line of sight from a point on the earth to a satellite can be characterized by its azimuth  $A$  and elevation  $E$ . These are defined in Fig. 4.1.

The azimuth is seen to be independent of the satellite altitude and is given by

$$\cot (\pi - A) = \sin \phi_P \cot (\Theta_P - \Theta_S) \quad (4.6)$$

in the northern hemisphere and by

$$\cot A = - \sin \phi_P \cot (\Theta_P - \Theta_S) \quad (4.7)$$

in the southern hemisphere. Although these forms are essentially identical, they are listed separately to insure that using principal

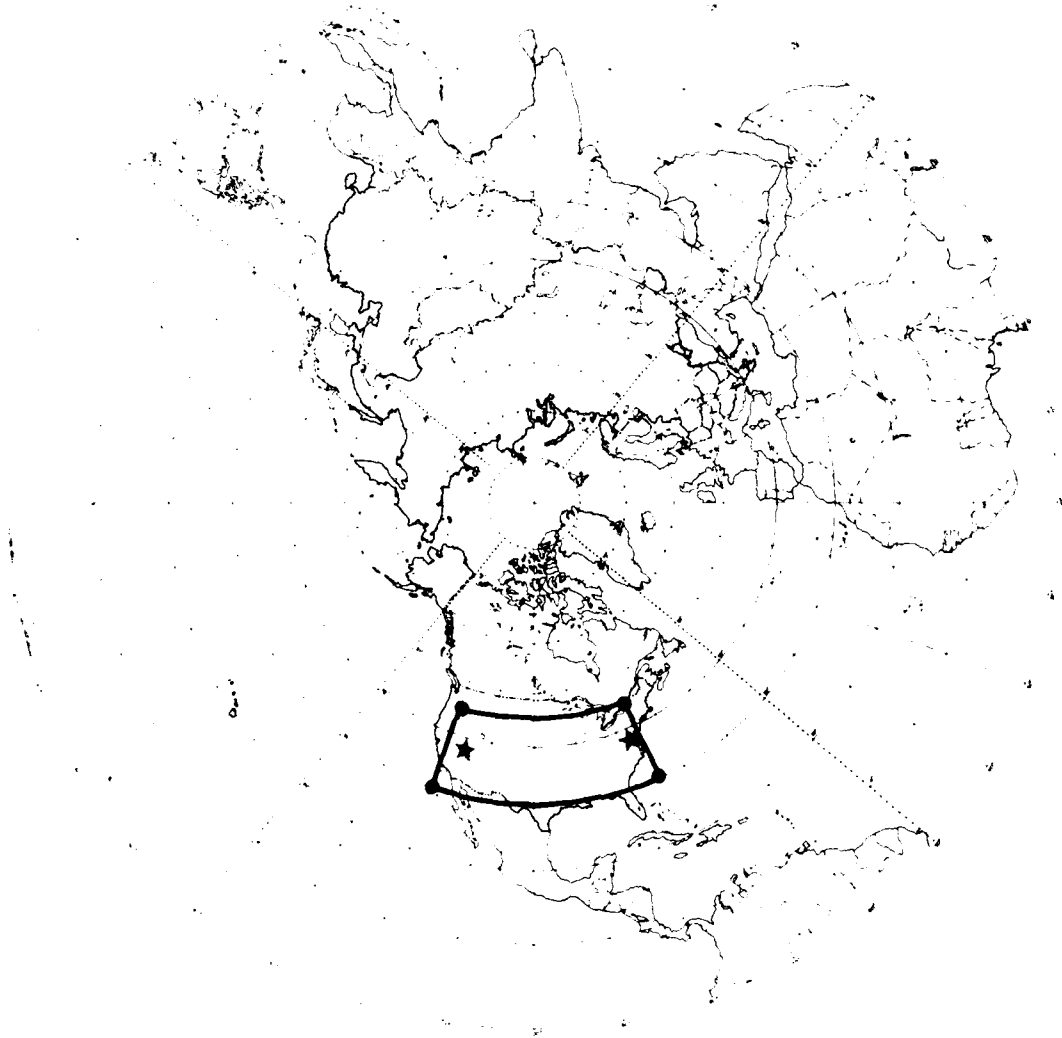


Fig. 4.5 — Generalized service area and user locations chosen to illustrate significant system parameters

values results in azimuths that are consistent with the definition.  
The elevation is given by

$$E = \frac{\pi}{2} - \theta - \epsilon \quad (4.8)$$

where  $\theta$  is given by Eq. (4.4) and  $\epsilon$  by Eq. (3.19).

Azimuth and elevation trajectories are plotted in Figs. 4.6a and 4.6b for users at latitudes of 30 and 45 deg north for the range of orbital altitudes from 3000 to 10,000 km. In general, for users in the northern hemisphere, the satellite rises from the south of west, reaches its maximum elevation when due south, then sets to the south of east.

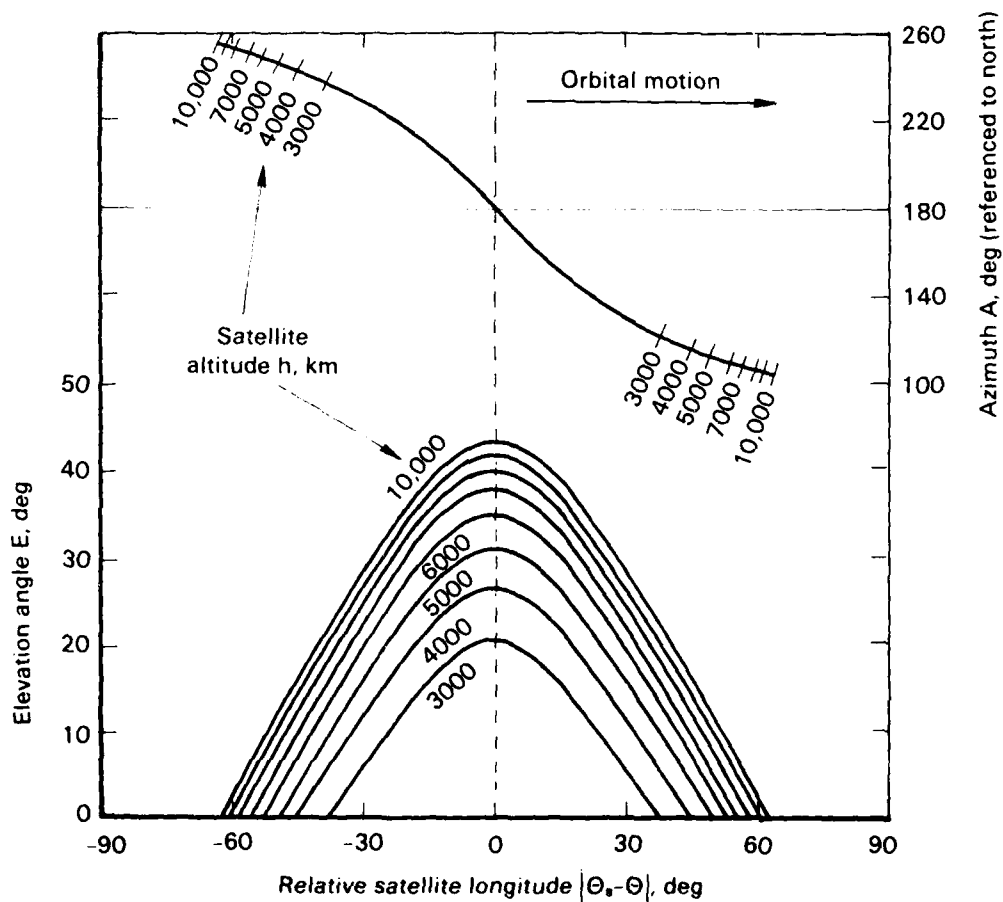


Fig. 4.6a — Azimuth and elevation trajectories for a satellite in a circular equatorial orbit as viewed by a user at 30 deg N latitude

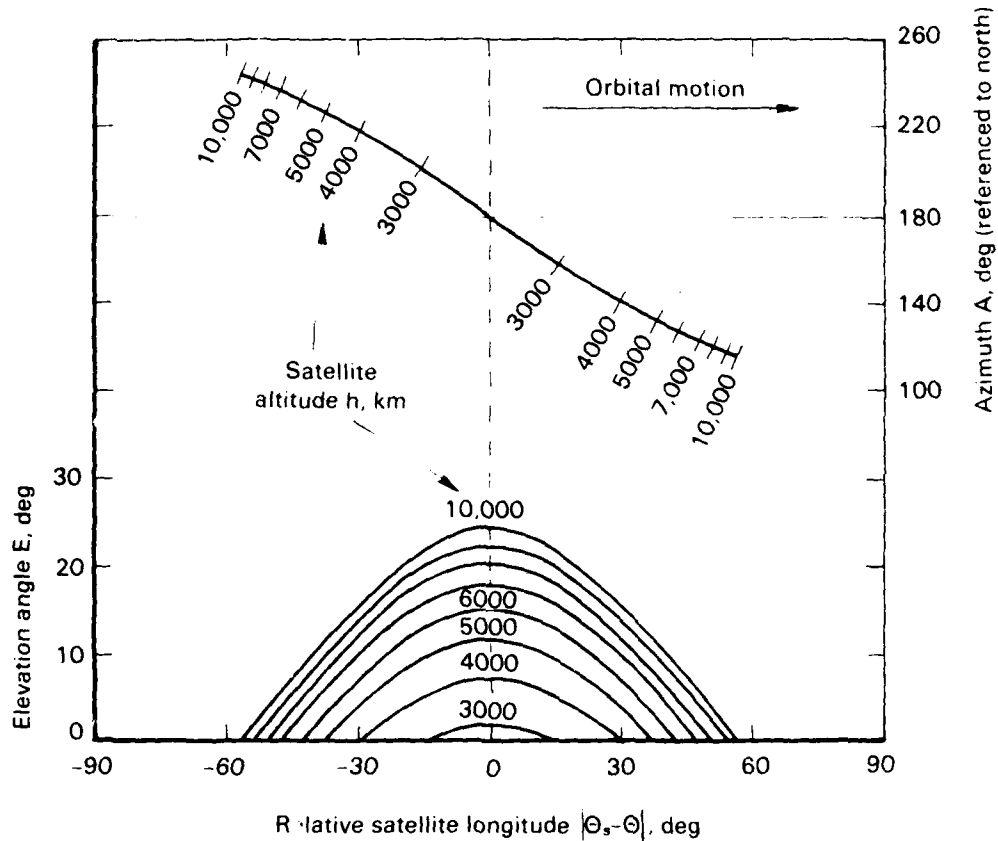


Fig. 4.6b — Azimuth and elevation trajectories for a satellite in a circular equatorial orbit as viewed by a user at 45 deg N latitude

#### Mutual Visibility

The coverage of interest for communication purposes is that within which the satellite is in view by a pair of users. Figure 4.4 can be used to determine if the users have mutual view of a satellite by seeing if they are both within the coverage area. Because of the relative motion of the satellite, the coverage area can be thought to rotate in a counterclockwise direction, i.e., toward the east, as the points denoting the users remain fixed on the projection grid. Conversely, the coverage area can be thought to remain fixed as the users rotate in a clockwise, or westerly, direction. By either method, the

relative longitude at which the satellite first appears in view of both users and then passes from view of both can be estimated.

The pairs of rising and setting relative satellite longitudes can also be calculated from Eq. (4.5) and the pair representing the extremes of mutual visibility selected by inspection. It should be noted that the satellite does not necessarily appear to either rise or set first as seen by the more westerly user. The more easterly user may observe the satellite to rise first if he is sufficiently nearer the equator; similarly, he may observe it to set first if he is sufficiently nearer the pole.

The arc of mutual visibility, i.e., the span of satellite longitudes over which the satellite is visible to both users, is shown in Figs. 4.7a to 4.7c for the user pairs designated above. As might be

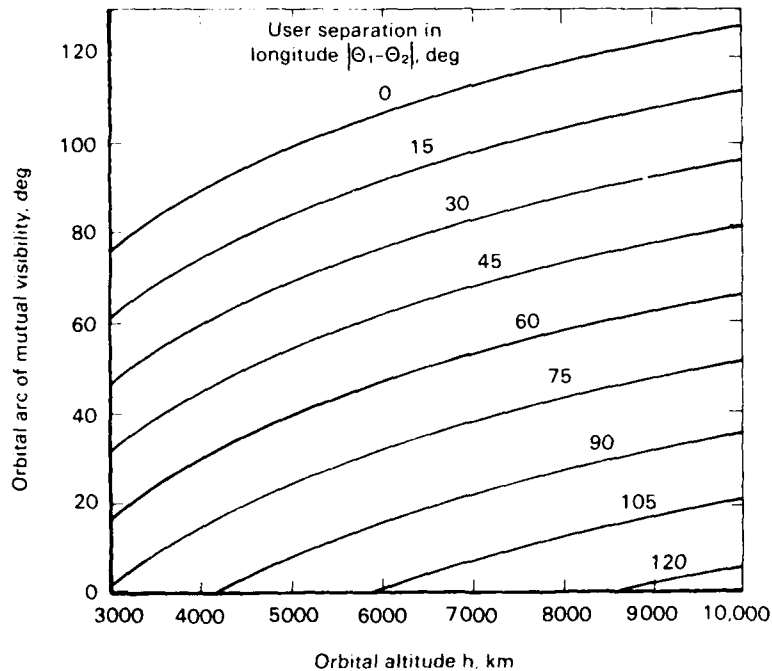


Fig. 4.7a - Arc of mutual visibility for a satellite in a circular equatorial orbit as viewed by users both at 30 deg latitude



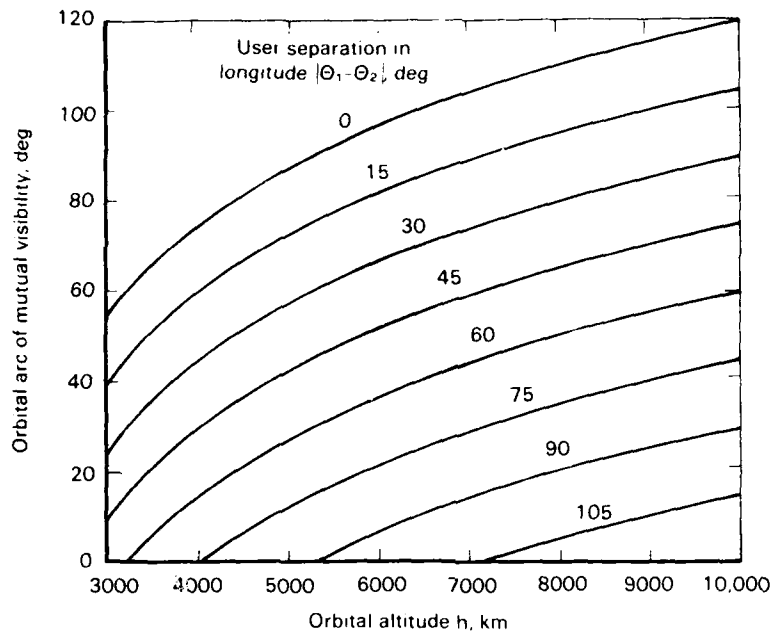


Fig. 4.7b — Arc of mutual visibility for a satellite in a circular equatorial orbit as viewed by one user at 30 deg latitude and the other at 45 deg latitude

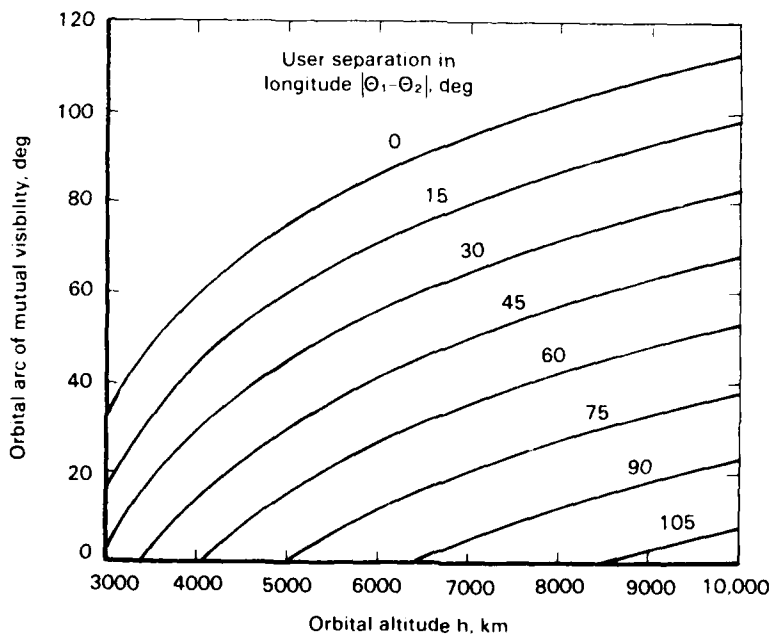


Fig. 4.7c — Arc of mutual visibility for a satellite in a circular equatorial orbit as viewed by users both at 45 deg latitude

expected, the arc of mutual visibility is greater for the users nearer the equator and increases as the satellite orbital altitude is raised or as the users are brought closer in longitude. Plots such as these are useful in estimating the minimum number of satellites required to maintain continuous coverage.

The mutual viewing time is obtained by applying the apparent orbital angular rate from Eq. (4.3) to the arcs of mutual visibility. These are presented in Figs. 4.8a to 4.8c for the same user pairs as above.

For user pairs at other locations, the arc of mutual visibility can be inferred from Fig. 4.4 by the procedure previously outlined. The mutual viewing time can then be calculated using the relative orbital angular rate from Fig. 4.3.

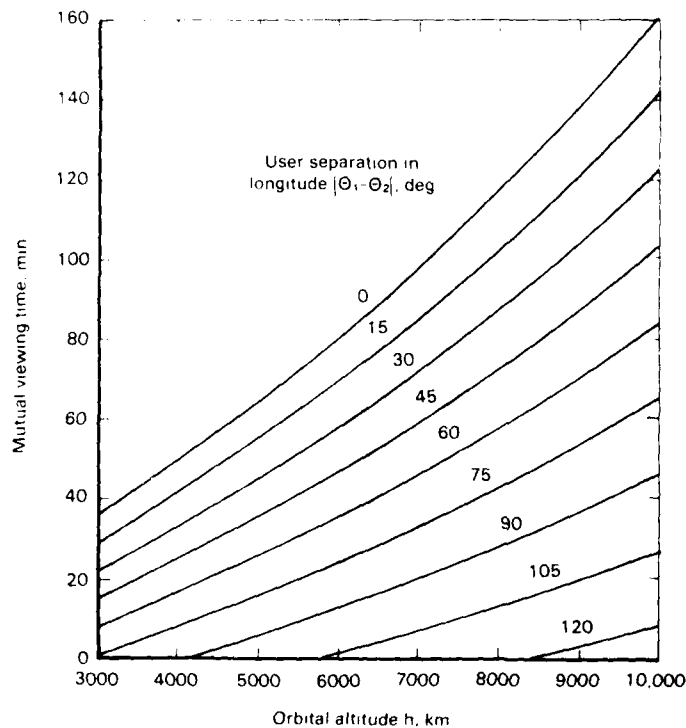


Fig. 4.8a — Mutual viewing time for a satellite in a circular equatorial orbit as viewed by users both at 30 deg latitude

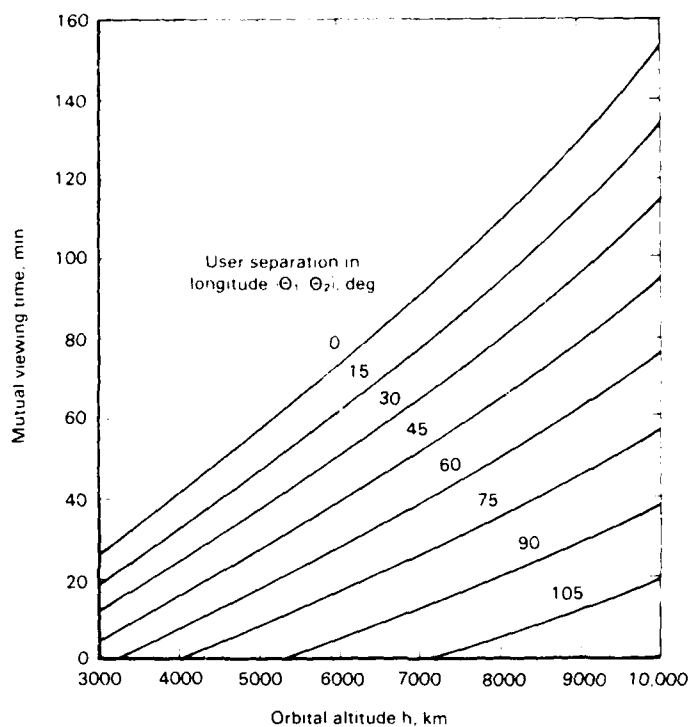


Fig. 4.8b — Mutual viewing time for a satellite in a circular equatorial orbit as viewed by one user at 30 deg latitude and the other at 45 deg latitude

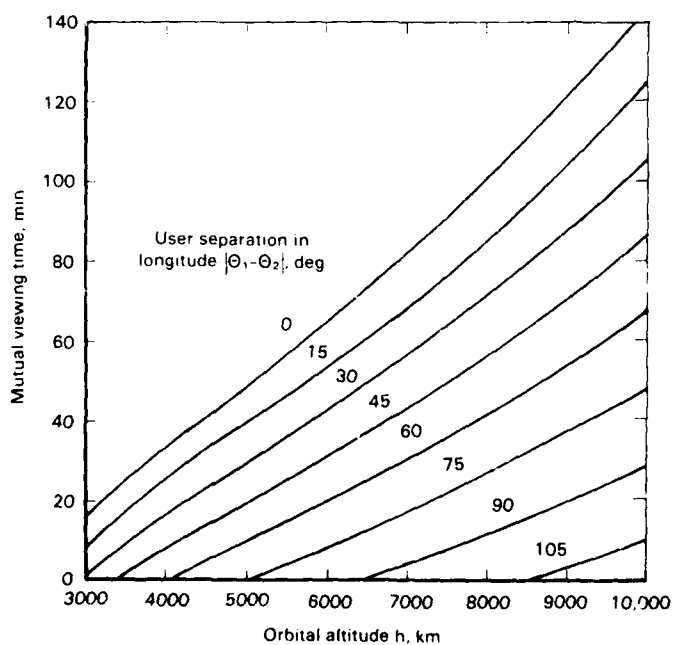


Fig. 4.8c — Mutual viewing time for a satellite in a circular equatorial orbit as viewed by users both at 45 deg latitude

## ARRAY OPERATING PARAMETERS

### Bistatic Scattering Angle

The relevance of the bistatic scattering angle to the scattering cross section of the array was established in Sec. II. It can be shown, from Fig. 4.1, to be given by

$$\cos \gamma = \frac{\ell_{01}^2 + \ell_{02}^2 - 4 R_e^2 \sin^2 (\Gamma/2)}{2 \ell_{01} \ell_{02}} \quad (4.9)$$

where the line-of-sight path lengths  $\ell_{01}$  and  $\ell_{02}$  to the center of the array are given by Eq. (3.18). The angle  $\Gamma$ , not shown in Fig. 4.1, is the central angle between the users and is given by

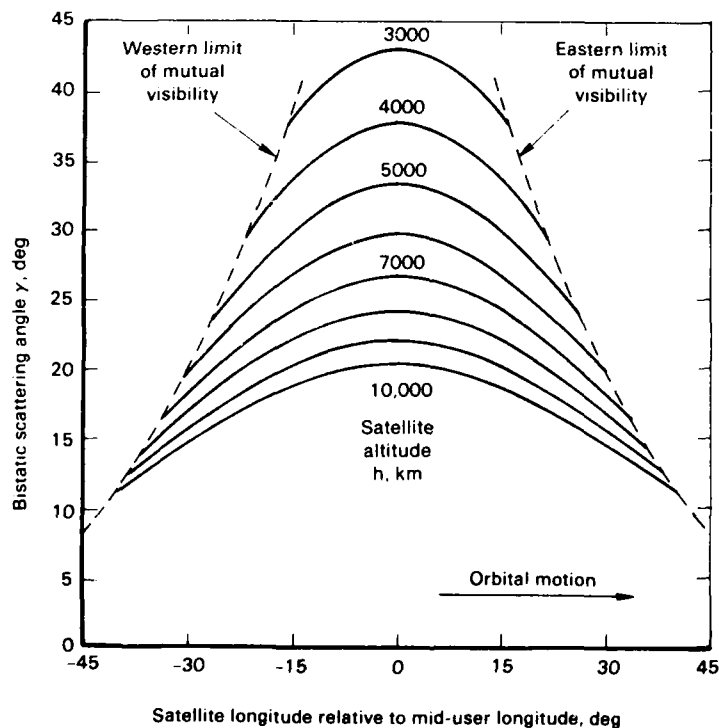


Fig. 4.9a — Bistatic scattering angle for a satellite in a circular equatorial orbit as viewed by users both at 30 deg latitude and separated by 45 deg in longitude

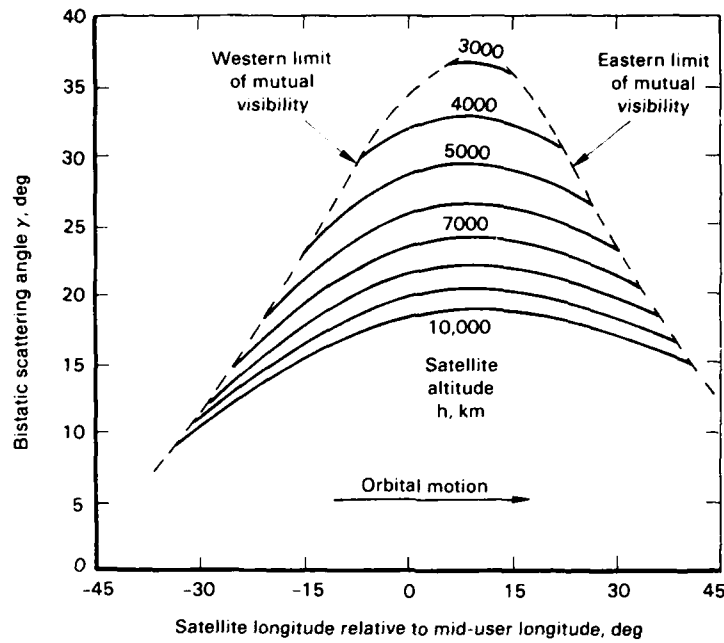


Fig. 4.9b — Bistatic scattering angle for a satellite in a circular equatorial orbit as viewed by one user at 30 deg latitude and the other at 45 deg longitude, separated by 45 deg in longitude

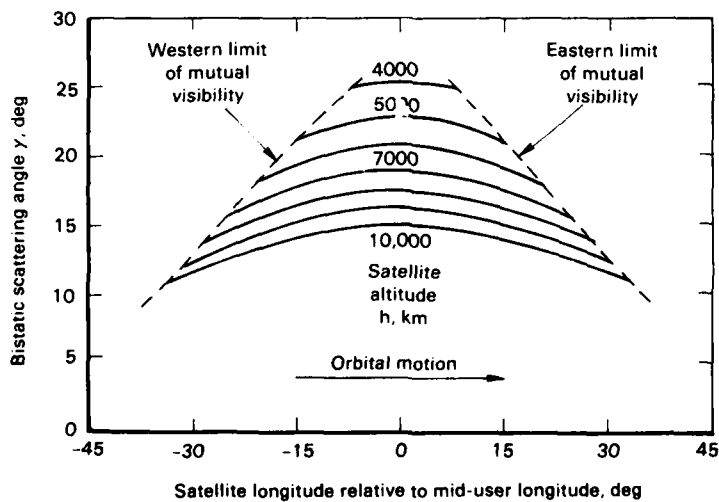


Fig. 4.9c — Bistatic scattering angle for a satellite in a circular equatorial orbit as viewed by users both at 45 deg latitude and separated by 45 deg in longitude

$$\cos \Gamma = \sin \phi_1 \sin \phi_2 + \cos \phi_1 \cos \phi_2 \cos (\theta_2 - \theta_1) \quad (4.10)$$

The bistatic scattering angle is shown in Figs. 4.9a to 4.9c as a function of satellite longitude relative to the midlongitude of a pair of users for a range of satellite orbital altitudes. The plots are for the three cases of the user pairs at the extremities of the generalized service area depicted in Fig. 4.5. When the users are at the same latitude, the maximum value of the bistatic scattering angle is reached when the satellite is midway between the users.

#### Operating Wavelength

It was shown in Eq. (3.41) that the operating wavelength  $\lambda_1$  required to form a link between a pair of users is given by

$$\lambda_1 = -s(h_1 + h_2) \quad (3.41)$$

where  $s$  is the element spacing and the  $h$ 's are given by the first of Eqs. (3.25). The quantities  $h_1$  and  $h_2$  are expressed in terms of the relevant geometrical factors illustrated in Fig. 3.3. The latitudes and longitudes of the users and the satellite can be introduced by using Eqs. (4.4), if desired. The end-fire operating wavelength  $\lambda_0$ , in Eq. (2.39), can be used to eliminate  $s$  yielding

$$\frac{\lambda_1}{\lambda_0} = -1/2 (h_1 + h_2) \quad (3.42)$$

The relationship expressed by Eq. (3.42) is purely geometric and does not include the dynamics of satellite and user motion. Thus, the equation is correct only when applied to the case of a geostationary, nonlibrating satellite as viewed by fixed users. In that event, the operating wavelength  $\lambda_1$  given by Eq. (3.42) is not only correct but is also constant and the same in both directions of propagation.

The Doppler shift introduced by user motion is familiar and easily accommodated. The effect of orbital motion is complex and will not be considered here; a detailed analysis will appear in a forthcoming report where its effects on signal acquisition and tracking are considered [7].\* Fortunately, the resulting difference in operating wavelength is small for the orbital altitudes of interest so that Eq. (3.42) is adequate for the purpose of estimating the total operating bandwidth that may be required.

The extremes of relative operating wavelength  $\lambda_1/\lambda_0$  and its equivalent  $f_1/f_0$  have been calculated using Eq. (3.42) and are shown in Figs. 4.10a to 4.10c as a function of libration angle for a range of satellite orbital altitudes. The computational procedure was to calculate the maximum and minimum values of  $\lambda_1/\lambda_0$  that were experienced during a fictitious satellite transit in which the tilt angle  $\psi$

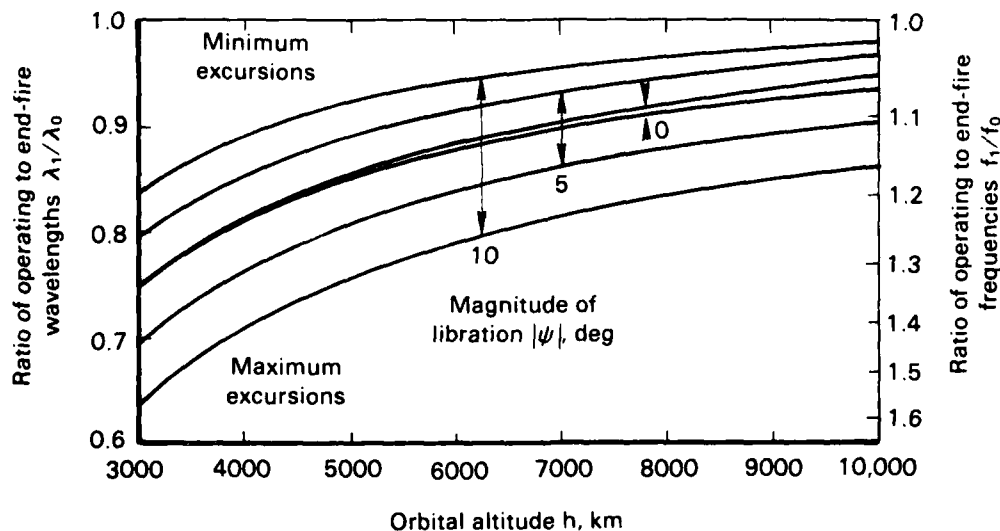


Fig. 4.10a — Extremes of operating wavelength and frequency for a librating PACSAT in a circular equatorial orbit as viewed by users both at 30 deg latitude and separated by 45 deg in longitude

\*The major consequence is that the path is no longer bilateral. Also, there is a Doppler smear, aggravated by libration, that develops because of differential Doppler shifts along the array.

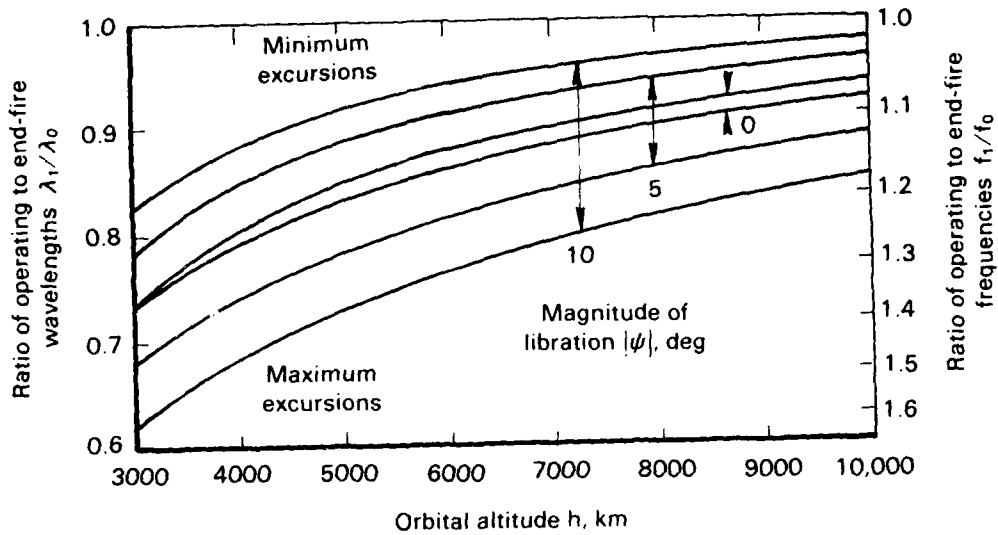


Fig. 4.10b — Extremes of operating wavelength and frequency for a librating PACSAT in a circular equatorial orbit as viewed by one user at 30 deg latitude and the other at 45 deg longitude, separated by 45 deg in longitude

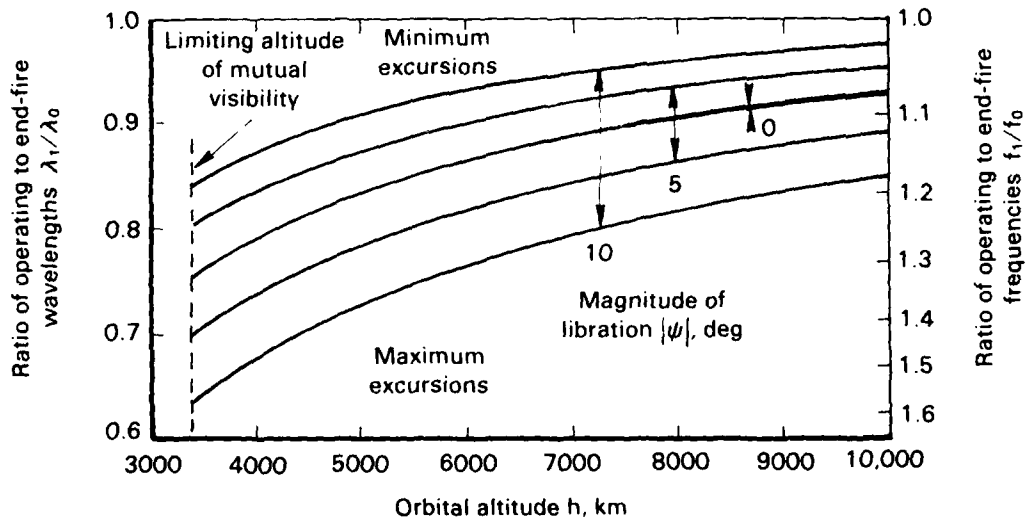


Fig. 4.10c — Extremes of operating wavelength and frequency for a librating PACSAT in a circular equatorial orbit as viewed by users both at 45 deg latitude and separated by 45 deg in longitude



was fixed in a given plane  $\omega$ . This was repeated over the 360 deg range of  $\omega$  to determine the extrema. (The existence of a spread in operating wavelength even when there is no tilt merely reflects the changing geometry characteristic of the basic satellite transit.)

This procedure obviously ignores the physics of libration. It simply determines the extremes of operating wavelength that might be experienced during the transit of a satellite with a given tilt angle  $\psi$  if it were allowed to assume all possible orientations  $\omega$ . The actual libration of a rigid body is much more complex. The motion can be resolved into in-plane and out-of-plane oscillations whose periods are equal, respectively, to  $1/\sqrt{3}$  and one-half the orbital period. The relative amplitudes and phases are different, in general, and are coupled in a complex manner. It suffices here to use the simple worst-case procedure to determine the maximum operating bandwidth required for a given tilt angle, which is loosely referred to as the libration angle.

The phenomenon of nearly constant operating wavelength alluded to in the introduction to this section is apparent from the no-libration cases in which the minima and maxima experienced during the course of a transit usually differ by much less than one percent. Introducing libration greatly increases the range of wavelengths that might be required. If, in addition, complete freedom of user locations within the satellite field of view were allowed, bandwidths of 20 to 30 percent or more would be required. A typical frequency allocation suitable for use by a passive satellite system is only 6 percent wide,\* so it is apparent that libration must be limited to only a few degrees at most and that some user geometries must be avoided. (The latter may not prove to be a serious limitation as it amounts to avoiding close user spacings and equatorial latitudes.) The higher orbital altitudes are clearly preferable from this point of view.

#### Typical Array Design

An expression for the scattering cross section of the PACSAT array in the far field was developed in Sec. II and is given by Eq.

---

\*7900 MHz to 84 MHz, earth-to-space, for example.

(2.37). Using Eq. (2.40), it can be brought into the form

$$\frac{\sigma}{L^2(a/\lambda_0)} = k_0 a \frac{\sigma_{LR}}{\pi a^2} \quad (4.11)$$

which is plotted in Fig. 2.6. The normalized scattering cross section of a sphere  $\sigma_{LR}/\pi a^2$  is obtained from Eq. (2.18) and is a function of the bistatic scattering angle, denoted by  $\theta$  in that section and by  $\gamma$  in this, and the dimensionless parameter

$$k_0 a = \frac{2\pi a}{\lambda} \quad (4.12)$$

where  $\lambda$  is the operating wavelength (see Eq. (2.2)) and  $a$  is the sphere radius. For computational purposes,  $\sigma_{LR}/\pi a^2$  is given by the polynomial Eq. (A.1) in the appendix.

A suitable form of the array scattering cross section for design purposes is  $\sigma/L^2$ , where  $L$  is the array length. To arrive at this from  $\sigma/L^2(a/\lambda_0)$ , it is necessary to specify the sphere radius  $a$  and the end-fire wavelength  $\lambda_0$ . The latter is related to the sphere spacing  $s$  by

$$s = \lambda_0/2 \quad (2.40)$$

Thus, if  $a$  and  $s$  (and hence  $\lambda_0$ ) were specified,  $\sigma/L^2$  could be calculated as a function of  $\lambda$  and  $\theta$  by bringing Eq. (4.11) into the form

$$\frac{\sigma}{L^2} = \frac{1}{2\pi} (k_0 a)^2 \frac{\sigma_{LR}}{\pi a^2} \left( \frac{\lambda}{\lambda_0} \right) \quad (4.13)$$

A typical design procedure for specifying  $a$  and  $s$  will be illustrated for a nonlibrating PACSAT intended to serve the area shown in Fig. 4.5. It is based on the desire to keep the system operating point, as determined by  $\lambda$  and  $\theta$ , as near as possible to the ridge marked on the surface of Fig. 2.6. The bistatic scattering angle  $\theta$  is, of course, fixed by the satellite-user geometry so that only the

normalized sphere size  $k_0 a$  is available for specification. Let the subscript, des, denote a value at a design point. Then

$$k_0 a = \frac{2\pi a}{\lambda} = \frac{2\pi a}{\lambda_{\text{des}}} \frac{\lambda_{\text{des}}}{\lambda_0} \frac{\lambda_0}{\lambda} = \frac{(k_0 a)_{\text{des}} (\lambda/\lambda_0)_{\text{des}}}{\lambda/\lambda_0} \quad (4.14)$$

The design value  $(k_0 a)_{\text{des}}$  will be selected by noting, from Fig. 2.6, that the array scattering cross section will be more or less optimized for lesser values of  $\theta$  if it lies on the ridge when  $\theta$  attains its maximum value. For users within the designated service area, this maximum occurs between users both at 30 deg latitude and separated by 45 deg in longitude and can be found from the plot in Fig. 4.9a. The design value  $(k_0 a)_{\text{des}}$  can then be read from the plot in Fig. 2.7.

The design value  $(\lambda/\lambda_0)_{\text{des}}$  should be selected to typify the average value that might be experienced by user pairs located anywhere within the service area. Failing an exhaustive search over possible user pair locations, an adequate approximation can be obtained from Figs. 4.10a to 4.10c by noting that there is little variation during the course of a satellite transit for a given user pair and that the results are not sensitive to the specific user pair locations considered. Therefore, the average value of  $\lambda/\lambda_0$  experienced by the user pair located at the opposite extremities of the service area, as given in Fig. 4.10b, will be used for the design value  $(\lambda/\lambda_0)_{\text{des}}$ .

The design values that result from this procedure are listed in Table 4.1 for reference. The orbital altitude of 3000 km is not considered because it does not allow coverage of the entire service area.

The design values from Table 4.1 and the operating wavelength ratio  $(\lambda/\lambda_0)$  from Eq. (3.42) can be used to determine  $k_0 a$  from Eq. (4.14). Then, using Eq. (4.9) for the bistatic scattering angle  $\theta$  and Eq. (A.1) for  $\sigma_{\text{LR}}/\pi a^2$ , the normalized scattering cross section  $\sigma/L^2$  is calculated from Eq. (4.13). The results are plotted in Figs. 4.11a to 4.11c for the user pairs at the extremities of the service area. The altitude dependence stems in part from the smaller bistatic scattering

Table 4.1

TYPICAL GENERALIZED PACSAT DESIGN PARAMETERS

Orbital Altitude $h$ , km	Maximum Bistatic Scattering Angle $\theta$ , deg	Design Normalized Sphere Size $(k_0 a)_{des}$	Design Operating Wavelength Ratio $(\lambda/\lambda_0)_{des}$
4000	37.86	1.1523	0.7980
5000	33.43	1.1412	0.8417
6000	29.80	1.1340	0.8718
7000	26.81	1.1287	0.8936
8000	24.32	1.1250	0.9103
9000	22.23	1.1221	0.9233
10,000	20.45	1.1200	0.9337

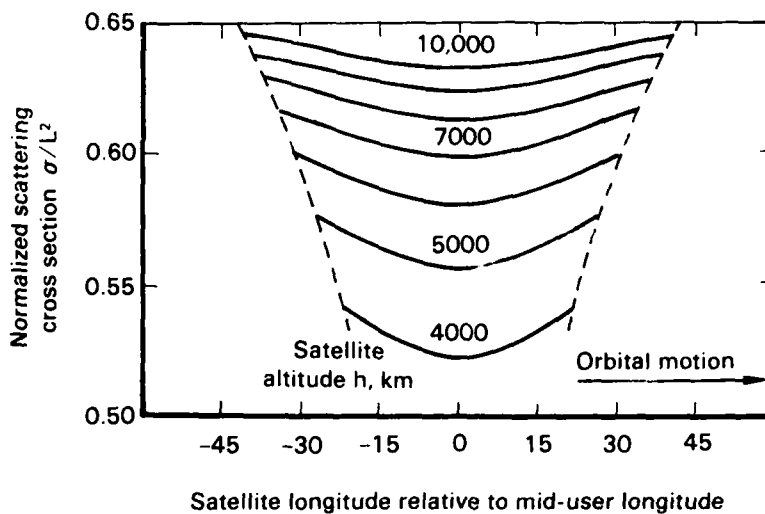


Fig. 4.11a — Normalized scattering cross section for a nonlibrating PACSAT in a circular equatorial orbit as viewed by users both at 30 deg latitude and separated by 45 deg in longitude

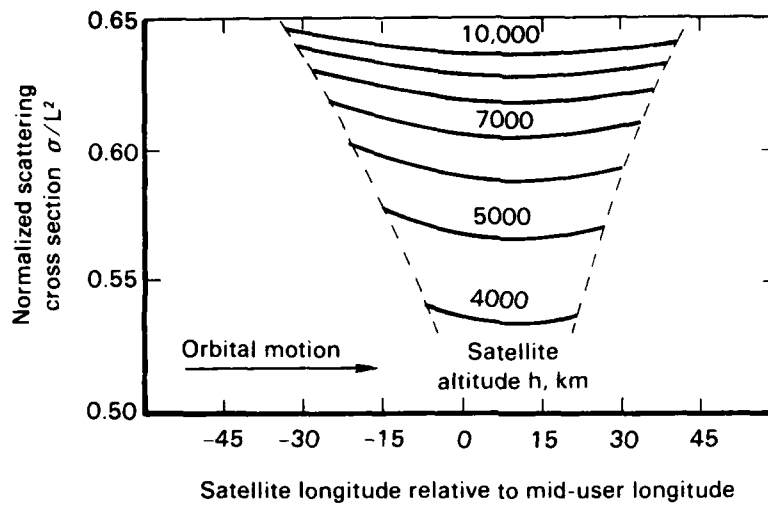


Fig. 4.11b — Normalized scattering cross section for a nonlibrating PACSAT in a circular equatorial orbit as viewed by one user at 30 deg latitude and the other at 45 deg latitude, separated by 45 deg in longitude

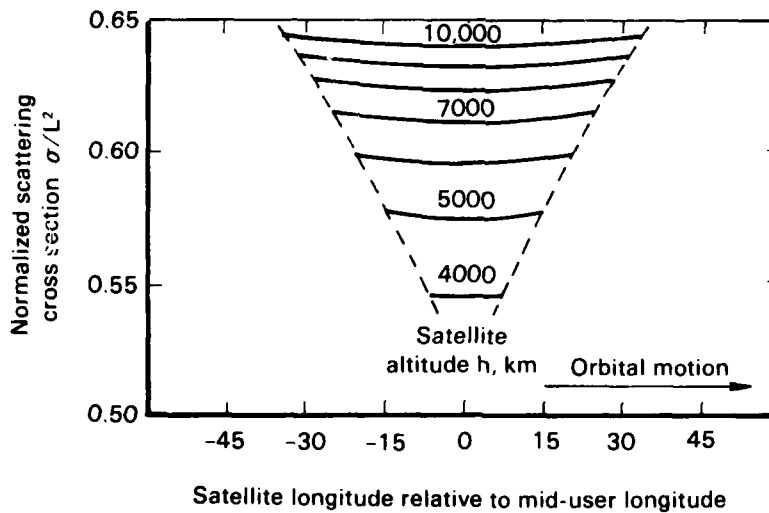


Fig. 4.11c — Normalized scattering cross section for a nonlibrating PACSAT in a circular equatorial orbit as viewed by users both at 45 deg latitude and separated by 45 deg in longitude

angles but mostly from the larger operating wavelength ratios experienced at the higher orbital altitudes. The variation with user pair location and relative satellite longitude is small at a given altitude. The approximation

$$\sigma = \cong 0.6L^2 \quad (4.15)$$

is probably adequate for rough estimates.

To illustrate a specific design, consider a system designed to operate in the 7900 to 8400 MHz band. Although this band is allocated for earth-to-space (i.e., uplink) use in the FIXED-SATELLITE service (i.e., between fixed terrestrial stations and an active satellite), it would be suitable for use by a passive satellite system on a noninterfering basis. The wavelength  $\lambda_{mid} = 3.681$  cm corresponding to the midband frequency 8150 MHz could then be used to determine the specific sphere size and spacing from the relationships

$$a = \frac{\lambda_{mid}}{2\pi} (k_0 a)_{des}, \quad s = \frac{\lambda_{mid}}{2(\lambda/\lambda_0)_{des}} \quad (4.16)$$

The values for sphere diameter  $d$  and spacing  $s$  corresponding to the values given in Table 4.1 are listed in Table 4.2.

Table 4.2

TYPICAL SPECIFIC PACSAT DESIGN PARAMETERS

Orbital Altitude h, km	Sphere Diameter d, cm	Sphere Spacing s, cm
4000	1.351	2.306
5000	1.337	2.186
6000	1.329	2.111
7000	1.322	2.060
8000	1.318	2.022
9000	1.315	1.993
10,000	1.312	1.971

The slow variation of sphere diameter with orbital altitude reflects the similarly slow variation of the optimum normalized sphere size with bistatic scattering angle displayed in Fig. 2.7. A departure from the listed value would cause the reduction in normalized scattering cross section associated with operating away from the area of the ridge in Fig. 2.6 and might therefore not be significant. A departure from the listed sphere spacing, however, would cause a change in the operating wavelength and that might have a significant impact on the ability of the system to remain within the allotted frequency band.

Though not pertinent to the topic of array design, it is convenient to list in Table 4.3 some of the interesting system parameters associated with the service area shown in Fig. 4.5. The minimum arc of mutual visibility is found from Fig. 4.7c and the minimum mutual viewing time from Fig. 4.8c for the user pair at the upper extremes of the service area; that is, both users at 45 deg latitude and separated by 45 deg in longitude. The maxima are found from Figs. 4.7a and 4.8a and for adjacent users at the lower edge of the service area; that is, both users at 30 deg latitude with no separation in longitude.

Table 4.3

TYPICAL PACSAT SYSTEM PARAMETERS

Orbital Altitude h, km	Arc of Mutual Visibility, deg		Mutual Viewing Time, min		Min. No. of Satellites Required
	Min.	Max.	Min.	Max.	
4000	14.3	89.6	7.9	49.7	26
5000	30.1	99.3	19.6	64.6	12
6000	41.4	107.0	31.3	80.7	9
7000	50.2	113.2	43.6	98.3	8
8000	57.3	118.4	56.8	117.4	7
9000	63.2	122.8	71.2	138.4	6
10,000	68.2	126.6	86.9	161.3	6

The minimum number of satellites required is the integer next larger than 360 divided by the minimum arc of mutual visibility. This

is equal to the number of satellites, which, if equally spaced about the orbital arc, will ensure that there will always be a satellite in mutual view of all users within the service area. Inasmuch as PACSAT will probably not have a station-keeping ability, the satellites will move with respect to one another because of initial errors in orbital injection velocity. Thus, a practical system will require more than the minimum number listed in Table 4.3 if continuity of service is to be assured. Anticipated drift rates and suitable replenishment strategies for preventing incipient gaps will be considered in a companion report.

#### COMMUNICATION CHARACTERISTICS

##### Line-of-Sight Path Length

The length of the line of sight from the user to the center of the array is given in Eq. (3.18). The maximum value of the central angle  $\theta$  is given by Eq. (3.17); for an equatorial orbit,  $\theta$  is related to the satellite longitude and the user latitude and longitude by Eq. (4.4), as illustrated in Fig. 4.1. The line-of-sight path length is given in the composite plot Fig. 4.12 as a function of these parameters.

The use of Fig. 4.12 is illustrated by the dashed lines. The plot is entered at the upper right at the difference between the satellite and user longitudes. At the intersection with the user latitude, the abscissa is followed downward to the intersection with the satellite altitude. The path length is then given by the lower-left-hand ordinate. As noted, the abscissa is the central angle  $\theta$ . Here, and in the following, the line-of-sight path length is designated by  $R$  rather than  $l_0$ .

##### The Link Equation

In Fig. 4.1, let the users be designated by the subscripts T and R, rather than 1 and 2, to denote that they are transmitting and receiving, respectively. Let  $P$  denote the transmitter power and  $G$  the gain of the antenna each is using. Then, the power transmitted in the



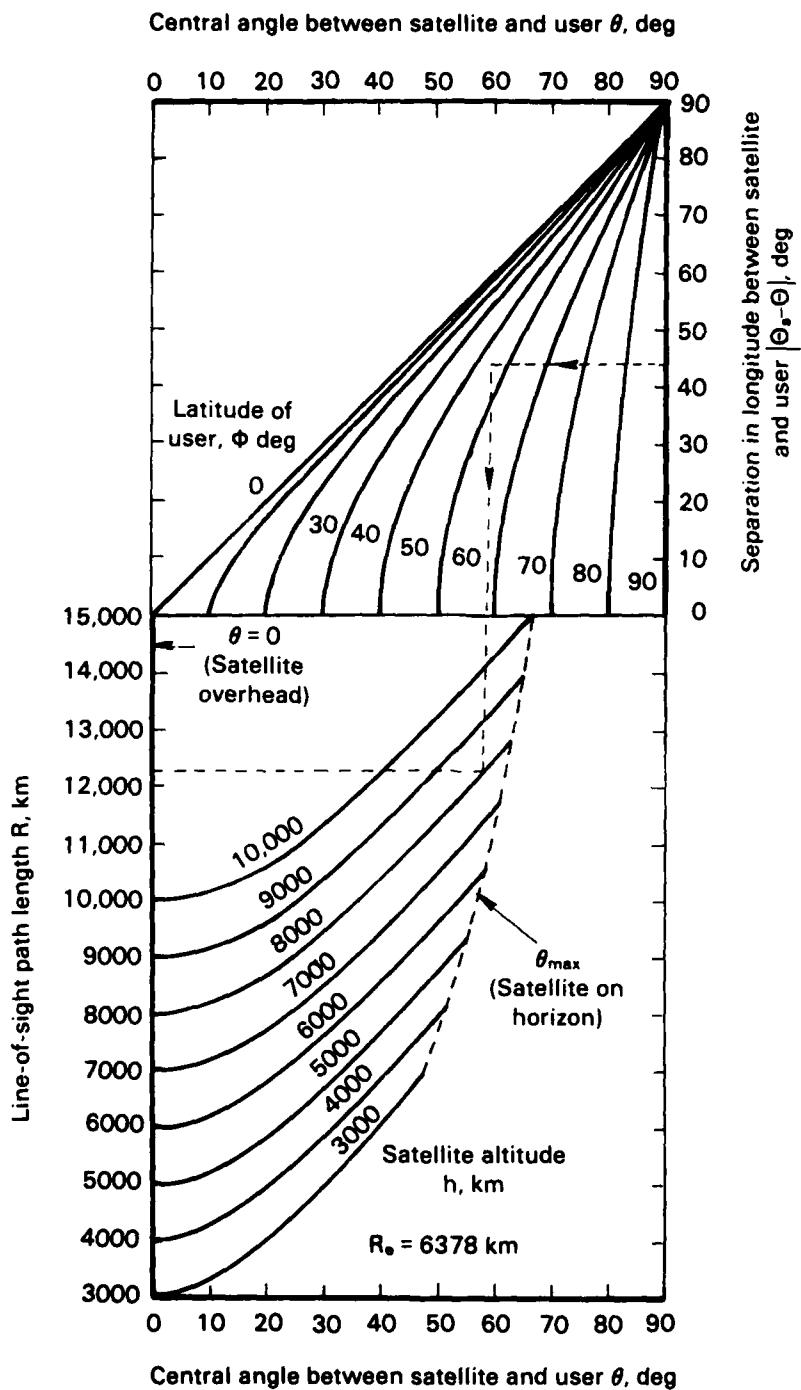


Fig. 4.12 — Line-of-sight path length to a satellite in an equatorial orbit

direction of the satellite is given by  $P_T G_T$  and the power density at the satellite by  $P_T G_T / 4\pi R_T^2$ . By definition, the array scatters a power  $P_T G_T \sigma / 4\pi R_T^2$  toward the receiver with unity again. Thus, the power density at the receiver is given by  $P_T G_T \sigma / (4\pi)^2 R_T^2 R_R^2$ . Let  $A_{R_{eff}}$  denote the effective capture cross section of the receiving antenna. The received power is then given by

$$P_R = \frac{P_T G_T \sigma A_{R_{eff}}}{(4\pi)^2 R_T^2 R_R^2 L} \quad (4.17)$$

where  $L$  is a loss factor ( $L > 1$ ) that accounts for pointing inaccuracies, circuitry, and path losses, etc., in practical systems.

Let  $R$  denote the signaling rate in bits per sec. Then, the bit duration is equal to  $1/R$  and the received energy per bit  $E_b$  is given by  $P_R/R$ . The system noise power spectral density  $N_0$  is given by

$$N_0 = kT \quad (4.18)$$

where  $k = 1.38054 \times 10^{-23}$  Joules per degree Kelvin and  $T$  is the system noise temperature. The received signal-to-noise ratio is then given by

$$\frac{E_b}{N_0} = \frac{P_R}{kTR} \quad (4.19)$$

Equation (4.19) can be written

$$P_R > P_{R_{min}} = \left( \frac{E_b}{N_0} \right)_{min} kTR \quad (4.20)$$

which states that the received power  $P_R$  must equal or exceed a minimum detectable value  $P_{R_{min}}$  that is related to the minimum usable signal-to-noise ratio  $(E_b/N_0)_{min}$ .

The factor  $M$  by which  $P_R$  exceeds  $P_{R_{\min}}$  is called the system margin. Introducing  $M$  and equating Eqs. (4.17) and (4.20) then leads to

$$M = \left( \frac{E_b}{N_0} \right)_{\min} k_{TR} = \frac{P_T G_T G_R A_{R_{\text{eff}}}}{(4\pi)^2 R_T^2 R_L^2} \quad (4.21)$$

which characterizes the performance of a passive communication link. The effective area of an antenna is related to its gain by the relationship

$$G = \frac{4\pi A_{\text{eff}}}{\lambda^2} \quad (4.22)$$

where  $\lambda$  is the operating wavelength. Thus Eq. (4.21) can also be written

$$M \left( \frac{E_b}{N_0} \right)_{\min} k_{TR} = \frac{P_T G_T G_R \lambda^2 \sigma}{(4\pi)^3 R_T^2 R_L^2} \quad (4.23)$$

For a circular parabolic dish antenna of diameter  $D$  the effective area is given by

$$A_{\text{eff}} = \eta \frac{\pi D^2}{4} \quad (4.24)$$

where  $\eta$  is an efficiency factor often taken as 0.55 for practical dishes. Then, Eq. (4.23) can be specialized to

$$M \left( \frac{E_b}{N_0} \right)_{\min} k_{TR} = \frac{\pi \eta_T \eta_R P_T D_T^2 D_R^2 \sigma}{64 \lambda^2 R_T^2 R_L^2} \quad (4.25)$$

### Typical Power Budgets

The large number of variables present in Eqs. (4.23) or (4.25) preclude the use of simple plots to illustrate system performance over a wide range of the parameters. The power budgets listed in Table 4.4 are therefore presented to show what results from using typical or practical values.

Table 4.4

#### TYPICAL PACSAT LINK PARAMETERS (PACSAT in circular equatorial orbit at 6000 km altitude)

Operating frequency	8 GHz	8 GHz
Transmitter power	5 kW	10 kW
Data rate	100 bps	1 kbps
Transmitter antenna diameter	75 cm	1 m
Range to transmitter	10,000 km	10,000 km
Scattering cross section	$10^6 \text{ m}^2$	$10^6 \text{ m}^2$
Range to receiver	10,000 km	10,000 km
System noise temperature	100 °K	100 °K
Losses, margin, and threshold	10 dB	10 dB
Receiver antenna diameter	70 cm	1.2 m

System operation was assumed to be in the 7.9 to 8.4 GHz band cited earlier. Data rates of 100 bps and 1 kbps were chosen as being representative of the data rates of interest in the military application to which PACSAT is suited. The path lengths were taken arbitrarily as 10,000 km; the path length to the horizon is 10,600 km for an orbital altitude of 6000 km (see Fig. 4.12). For convenience, the PACSAT scattering cross section was taken as  $10^6 \text{ m}^2$ , which corresponds to that for an array about 1300 m long (see Eq. (4.15)). The losses, margin, and threshold  $LM (E_b/N_0)_{\min}$  were lumped into a single factor, taken (perhaps optimistically) as 10 dB. The encouraging aspect of the power budgets listed in Table 4.1 is that they indicate that the link can be supported using reasonable transmitter powers and antenna sizes. Components such as these can readily be accommodated on large aircraft and mobile ground terminals.

Appendix  
FIFTH-ORDER R.M.S. POLYNOMIAL FIT TO MIE SOLUTION  
EXPANSION FOR ELECTROMAGNETIC SCATTERING FROM  
A PERFECTLY CONDUCTING SPHERE

Mr. V. V. Liepa of the Radiation Laboratory at the University of Michigan at Ann Arbor provided calculations of the real and imaginary parts of  $S_1(\theta)$  and  $S_2(\theta)$ . These were used to calculate  $\sigma_{LR}/\pi a^2$  from Eq. (2.18) for  $k_0 a = 0.9(0.1)1.4$  and  $\theta = 0(10)50$  deg. A uniformly weighted, least-mean-square, fifth-order polynomial in  $k_0 a$  and  $\theta$  was fitted to these points to facilitate computation at intermediate points. The polynomial is given by

$$\begin{aligned} \sigma_{LR}/\pi a^2 = & 81.376\ 862\ 28 - 6.440\ 739\ 782\ \theta - 417.915\ 971\ 2\ k_0 a \\ & + 14.772\ 132\ 26\ \theta^2 + 26.659\ 069\ 49\ \theta\ k_0 a + 814.742\ 881\ 3\ (k_0 a)^2 \\ & + 0.361\ 421\ 426\ 2\ \theta^3 - 42.417\ 652\ 88\ \theta^2\ k_0 a - 40.368\ 661\ 59\ \theta(k_0 a)^2 \\ & - 741.250\ 998\ 2\ (k_0 a)^3 + 0.918\ 550\ 083\ 2\ \theta^4 - 0.832\ 943\ 049\ 2\ \theta^3 k_0 a \quad (A.1) \\ & + 35.335\ 055\ 63\ \theta^2(k_0 a)^2 + 26.552\ 039\ 64\ \theta(k_0 a)^3 + 320.020\ 340\ 2\ (k_0 a)^4 \\ & + 0.040\ 049\ 287\ 89\ \theta^5 - 0.944\ 447\ 017\ 0\ \theta^4 k_0 a + 0.463\ 573\ 159\ 1\ \theta^3(k_0 a)^2 \\ & - 8.716\ 149\ 189\ \theta^2(k_0 a)^3 - 6.410\ 860\ 956\ \theta(k_0 a)^4 - 53.335\ 225\ 21\ (k_0 a)^5 \end{aligned}$$

where  $\theta$  is in radians. The r.m.s. error of the polynomial at the 36 fitting points is  $5.38 \times 10^{-4}$ ; the largest error is  $-1.084 \times 10^{-3}$ , the smallest,  $1.934 \times 10^{-5}$ . The polynomial was used directly to plot  $\sigma_{LR}/\pi a^2$  in Fig. 2.2; in accordance with Eqs. (2.38) and (2.41), it was simply multiplied by  $k_0 a$  to plot  $\sigma/L^2(a/\lambda_0)$  in Fig. 2.6.

REFERENCES

1. Yater, J. C., "Signal Relay Systems Using Large Space Arrays," *Trans. IEEE*, Vol. COM-20, No. 6, pp. 1108-1121, December 1972.
2. Bedrosian, E., *PACSAT: A Passive Communication Satellite for Survivable Command and Control*, The Rand Corporation, N-1780-ARPA, November 1981.
3. Mie, G., "Beiträge zur Optik trüber Medien, speziell kolloidaler Metallösungen," *Annalen der Physik*, Vol. 25, No. 377, 1908.
4. Stratton, J. A., *Electromagnetic Theory*, Sections 9.25-9.27, McGraw-Hill, New York, 1941.
5. Barrick, D. E., *Radar Cross Section Handbook*, "Spheres," Chap. 3, G. T. Ruck, Ed., Vol. 1, Plenum Press, New York, 1970.
6. Richardus, P., and R. K. Adler, *Map Projections*, North-Holland Publishing Co., Amsterdam, 1972.
7. Bello, Phillip, "PACSAT Modem Design Considerations," CNR, Inc., Needham, Massachusetts (forthcoming).

PRECEDING PAGE BLANK-NOT FILMED